MULTISCALE MODEL. SIMUL.
Vol. 5, No. 3, pp. 695–728

TWO-DIMENSIONAL BULK MICROFLOW SIMULATIONS BASED ON REGULARIZED GRAD'S 13-MOMENT EQUATIONS*

MANUEL TORRILHON†

Abstract. The newly derived fluid model named regularized 13-moment system (R13) is capable of describing rarefied/microflows with high accuracy due to special modeling of the nonequilibrium dissipation. Explicit two-dimensional equations are presented and discussed and a specialized numerical method derived. In two dimensions evolution equations for nine basic variables need to be solved, including directional temperatures, shear stress, and heat flux. The governing partial differential equations are given in balance law form with relaxation and parabolic dissipation. The numerical method is formulated as a practical and straightforward extension of standard finite volume methods. It focuses on bulk simulations with no boundary in order to provide a building block. As a microflow example the interaction of a shock front with a dense microbubble is considered in which the bubble's diameter is a few mean free paths. The results are compared to the solution of the Navier–Stokes–Fourier system demonstrating the relevance of the new R13 model.

Key words. rarefied gases, continuum model, finite volume simulation, moment method

AMS subject classifications. 76P05, 76M12

DOI. 10.1137/050635444

1. Introduction.

The accurate modeling and simulation of nonequilibrium processes in rarefied fluids or microflows is one of the main challenges in present fluid mechanics. The traditional models developed centuries ago are known to lose their validity in extreme physical situations. In these models the nonequilibrium variables, stress and heat flux, are coupled with gradients of velocity and temperature as given in the constitutive relations of Navier–Stokes and Fourier (NSF). However, in rarefied fluids or microflows away from equilibrium the inertia and higher order multiscale relaxation in the fluid become dominant and essential; see the textbook [23].

It is generally accepted that kinetic theory based on a statistical description of the gas provides a valid framework to describe processes in a rarefied regime or at small scales. Introductions into kinetic theory and its core, Boltzmann equation, can be found in many textbooks; see, e.g., [11] or [46]. The main variable used to describe the gas is the distribution function or probability density of the particle velocities. This statistical description is also used in the direct simulation Monte Carlo (DSMC) method as described in the textbook [6]. However, in many situations the detailed statistical approach yields a far too complex description of the gas. It turns out to be desirable to have a continuum model based on partial differential equations for the fluid mechanical field variables. This model should accurately approximate the multiscale phenomena present in kinetic gas theory in a stable and compact system of field equations.

The approximation strategies in kinetic theory range from Chapman–Enskog expansion and Burnett models to Grad's moment method and extended thermodynamics. An overview is given in section 2. This paper uses the regularized 13-moment

*Received by the editors July 8, 2005; accepted for publication (in revised form) April 12, 2006; published electronically September 12, 2006. This work was supported by the German National Science Foundation (Deutsche Forschungsgemeinschaft, DFG) and the Research Grants Council (RGC) of Hong Kong.

http://www.siam.org/journals/mms/5-3/63544.html

†Department of Mathematics, Hong Kong University of Science and Technology, Clear Water Bay, Kowloon, Hong Kong (matorril@ust.hk).

system (R13) derived by Struchtrup and Torrilhon in [40]. Based on kinetic theory the R13 system provides a continuum model for rarefied/microflow which is of higher accuracy than other models, with smooth solutions and stable evolution in contrast to Burnett models. It consists of evolution equations for the fluid fields density, velocity, temperature, stress tensor, and heat flux. Equivalently, instead of the stress tensor in the basic variables set, it can be viewed to include the three directional temperatures and shear stresses. The evolution equations are of hyperbolic-parabolic form with relaxation. The relaxational and parabolic part is present only in the equations of stress and heat flux and models the multiscale dissipation of Boltzmann's equation; see [40]. As the Boltzmann equation the R13 system is derived for monatomic gases, and all the results in this paper are restricted to this case. The extension to polyatomic gases or mixtures is reserved for future work.

So far, the R13 system was derived in fully three-dimensional form, but test cases were considered only in one dimension. Comparison to other models was conducted by Torrilhon and Struchtrup in [44] in the case of shock wave profiles. This paper presents the first two-dimensional results. Therefore, the two-dimensional equations are discussed and presented in a fully explicit way in balance law form suitable for common numerical methods. We will thoroughly derive an accurate and robust numerical method designed for time dependent problems and present several numerical experiments. The method handles a transport flux, a relaxation, and a dissipative gradient coupled in a single standard finite volume method. The coupling is considered to be important since the solutions arise from a complex interplay of transport, relaxation, and dissipation in the model. Stability and order of convergence of the proposed method is investigated in numerical experiments and empirical error calculations.

As a two-dimensional microflow example we consider a shock wave interaction with a dense bubble. In different simulations the diameter of the bubble is considered to be 100, 20, and 10 mean free paths of the gas. As the shock front crosses the bubble the front is distorted, inducing an additional nonequilibrium and nonuniform flow. For small bubble diameters classical fluid models lose their validity, and the R13 system is expected to provide a physically more accurate solution. To demonstrate this behavior the shock-bubble simulation is repeated but based on the NSF equations. The differences are shown and discussed in detail.

A main challenge for higher order fluid models are the correct choices of boundary conditions. For the NSF system, so-called slip boundary conditions are available; see, e.g., the textbook [35]. The question of boundary conditions for the R13 system is completely ignored in this paper, which must be considered as first step. After a practical two-dimensional numerical method for the bulk equations has been established the incorporation of boundary conditions will be the next step. Promising approaches would be a hybrid coupling between kinetic models or particle simulations and the R13 system in the vicinity of the boundary, as is done for other continuum models; see, e.g., [33] or [41]. The differences between the higher order R13 model and NSF presented in this paper are not influenced by the choice of boundary conditions and must be attributed to the poor nonequilibrium modeling inside the NSF system.

The rest of the paper is organized as follows: The next section comments on the different approaches of how to derive continuum models from kinetic theory and the derivation of the regularized 13-moment system. Section 3 introduces the R13 system in three-dimensional tensor notation and provides a balance law formulation and the explicit two-dimensional equations. The relation to NSF and Boltzmann's equation will be discussed, and investigations of the propagation speeds in two dimensions are

presented. Section 4 derives the numerical method after discussing general approaches in the beginning. Consecutively, the transport flux and the relaxation and the dissipative gradients are treated. Numerical experiments are conducted in section 5, where second order convergence rates are demonstrated in both one and two dimensions and different parameter settings. Section 6 presents the results for the shock-bubble interaction based on the R13 system and the comparison to NSF. The paper finishes with a conclusion.

2. Continuum models in kinetic theory. The main approximation tool of kinetic theory is based on asymptotic expansion of the distribution function in powers of the Knudsen number. The Knudsen number Kn is the dimensionless scaling parameter entering Boltzmann's equation. It represents the ratio of the microscopic mean free path of the particle and a macroscopic characteristic length. The Knudsen number becomes large for rarefied gases or microflows. In the limit $Kn \to 0$ the asymptotic analysis conducted in the Chapman–Enskog expansion leads to the classical NSF relations, including specific expressions of the transport coefficients; see the textbooks [11], [46].

The Chapman–Enskog expansion can be used to derive higher order constitutive relations from the Boltzmann equation. The resulting equations are called Burnett equations for the second order and super-Burnett in the case of the third order. They incorporate ever higher gradients of temperature and velocity into the constitutive relations for stress and heat flux. The relations of super-Burnett order for the full Boltzmann equation are already forbiddingly complex, and higher order was never considered. Furthermore, in general the corrections of higher than first order, i.e., Burnett and super-Burnett relations, are known to be unstable, as shown by Bobylev in [7]. In special cases the Burnett equations have been used to calculate higher Knudsen number flow, for example by Agarwal, Yun, and Balakrishnan in [2, 3], Lockerby and Reese in [28], or Xu and Li in [48]. In some cases the instability of Burnett equations could be overcome by ad-hoc modifications as in [49] by Zhong, MacCormack, and Chapman or in [47] by Xu. However, general stable Burnett relations that follow rigorously from the Boltzmann equation seem not to exist.

An alternative approximation strategy in kinetic theory is given by Grad's moment method based on Hilbert expansion of the distribution function in Hermite polynomials. The method is described by Grad in [15] and [16]. In contrast to Chapman–Enskog and Burnett this method extends the set of variables of a possible continuum model beyond the fields of density, velocity, and temperature. The additional variables are given by higher moments of the distribution function. The 13-moment case of Grad considers evolution equations for density, velocity and temperature, *and* stress tensor and heat flux. Higher moment theories include more moments which lack physical intuition. In the context of phenomenological thermodynamics extended theories proved to be successful in many test cases; see the textbook [29] of Müller and Ruggeri or, e.g., [20] by Jou, Casas-Vazquez, and Lebon.

Large moment systems with hundreds of variables were used to describe shock structures; see the dissertation [4] of Au, the shock-tube experiment in the work [5] by Au, Torrilhon, and Weiss, and heat conduction in [37] by Struchtrup. A computationally useful approach to large moment systems is using comulant theory; see [34] by Seeger and Hoffmann. However, even though the capability of Grad's moment method is assured by these results, its usefulness is restricted due to slow convergence. Indeed, many moments are needed to describe high nonequilibrium which results in large systems of partial differential equations to be solved.

Moment systems provide a rich mathematical structure discussed, e.g., in [29] by Müller and Ruggeri and in [26] by Levermore. It has been argued that evolution equations in physics should always be hyperbolic in order to provide a finite speed of propagation. In principal the moment systems lead to stable hyperbolic equations; however, in practical explicit systems hyperbolicity is given only in a finite range; see also the work [21] by Junk on this issue. Furthermore, the hyperbolicity leads to discontinuous subshock solutions in the shock profile. A variant of the moment method has been proposed by Eu in [13] and is used, e.g., in [31] by Myong. Recently, a 10-moment system has been used by Suzuki and van Leer in [42].

Both fundamental approaches of kinetic theory, Chapman–Enskog and Grad, exhibit severe disadvantages. Higher order Chapman–Enskog expansions are unstable, and Grad's method introduces subshocks and shows slow convergence. It seems to be desirable to combine both methods in order to remedy their disadvantages. Such a hybrid approach has already been discussed by Grad in a side note in [16]. He derives a variant of the regularized 13-moment equations given below, but surprisingly he neither gives any details nor does he use or investigate the equations. In the last 50 years his paper [16] was cited as standard source for introduction into kinetic theory, but, apparently, this specific idea got entirely lost and seems not to be known in present day literature.

The Chapman–Enskog expansion is based on equilibrium, and the corrections describe the nonequilibrium vicinity. A hybrid version which uses a nonequilibrium as its basis is discussed in [22] by Karlin et al. They deduced linearized equations with unspecified coefficients. Starting from Burnett equations Jin and Slemrod in [18] derived a extended system of evolution equations which resembles the regularized 13-moment system. It is solved numerically in [19] by Jin, Pareschi, and Slemrod. However, the tensorial structure of their relations is not in accordance with Boltzmann's equation. Starting from higher moment systems in [30] Müller, Reitebuch, and Weiss discussed a parabolization which incorporates higher order expressions into hyperbolic equations.

The regularized 13-moment equations used in this paper were rigorously derived from Boltzmann's equation in [40] by Struchtrup and Torrilhon. They discussed the relations to Burnett models and proved linear stability of the derived system. The key ingredient is a Chapman–Enskog expansion around a pseudoequilibrium which is given by the constitutive relations of Grad for stress tensor and heat flux. The procedure adds second order derivatives to Grad's evolution equations of stress and heat flux, thus regularizing the former hyperbolic equations into a mixed hyperbolic-parabolic system. Torrilhon and Struchtrup showed in [44] that the R13 system is in third order correspondence with Boltzmann's equation in powers of Kn. Thus, it must be viewed to be on the super-Burnett level. In [44] also shock profile calculations are presented and compared to results of other methods and to DSMC simulation results. R13 gives smooth shock profiles and shows superior agreement and stability properties. The theoretical background of the derivation of the system has been investigated and extended by Struchtrup in [38] and [39]. The textbook [36] by Struchtrup provides an introduction to approximation methods in kinetic theory, including the regularized moment equations.

3. Regularized Grad's 13-moment equations. The derivation of the regularized Grad's 13-moment equations for monatomic gases considered in this paper have been discussed by Struchtrup and Torrilhon in [40]. Comparisons and investigations of the physical approximation abilities, especially for shock profiles, are conducted in [44].

So far, the equations have been derived in condensed three-dimensional tensor notation. In the following section we will present equivalent formulations, such as balance law form, suitable for common numerical methods. Fully explicit and detailed equations are given for the two-dimensional case.

3.1. Full equations.

3.1.1. Variables. Originating from kinetic gas theory all variables of the R13 equations are based on moments of the particle velocity distribution function $f(\mathbf{x}, t, \mathbf{c})$. The mass density

$$\rho(\mathbf{x}, t) = m \int_{\mathbb{R}^3} f(\mathbf{x}, t, \mathbf{c})\, d\mathbf{c} \tag{1}$$

as well as the velocity and internal energy

$$v_i(\mathbf{x}, t) = \frac{m}{\rho(\mathbf{x}, t)} \int_{\mathbb{R}^3} c_i\, f(\mathbf{x}, t, \mathbf{c})\, d\mathbf{c}, \quad \varepsilon(\mathbf{x}, t) = \frac{m}{\rho(\mathbf{x}, t)} \int_{\mathbb{R}^3} \frac{1}{2}\,(c_i - v_i)^2\, f(\mathbf{x}, t, \mathbf{c})\, d\mathbf{c} \tag{2}$$

form the basic equilibrium variables of the gas. The pressure is given by $p = \frac{2}{3}\rho\varepsilon$ due to the assumption of monatomic gases, and we will use the temperature θ in energy units, i.e., $p = \rho\theta$. The R13 system describes the state of the gas by including the first two nonequilibrium variables, stress tensor and heat flux,

$$\sigma_{ij}(\mathbf{x}, t) = m \int_{\mathbb{R}^3} C_{\langle i} C_{j\rangle}\, f(\mathbf{x}, t, \mathbf{C})\, d\mathbf{C}, \quad q_i(\mathbf{x}, t) = m \int_{\mathbb{R}^3} \frac{1}{2} C_i C^2\, f(\mathbf{x}, t, \mathbf{C})\, d\mathbf{C} \tag{3}$$

which are based on the microscopic velocity $C_i = c_i - v_i$. Angular brackets denote the deviatoric (trace-free) and symmetric part of a tensor. The R13 equations are evolution equations for (1)–(3).

We will mostly use indexed quantities to describe vectors and tensors and summation convention for operations between them. Bold letters will be used in occasional invariant formulations. The Kronecker symbol δ_{ij} denotes the identity matrix $\mathbf{I}$. The stress tensor is related to the pressure tensor p_{ij} by $p_{ij} = p\delta_{ij} + \sigma_{ij}$, which will be used frequently. In addition to the angular brackets normal brackets are used to abbreviate the normalized sum of index-permutated tensor expressions.

3.1.2. Evolution equations. The evolution equations for density, velocity, and internal energy are given by the conservation laws of mass, momentum, and energy,

$$\begin{aligned} \partial_t \rho + \operatorname{div}(\varrho \mathbf{v}) &= 0, \\ \partial_t \rho\mathbf{v} + \operatorname{div}\left(\rho \mathbf{v}\mathbf{v}^T + p\mathbf{I} + \sigma\right) &= 0, \\ \partial_t\left(\rho\varepsilon + \tfrac{1}{2}\rho v_i^2\right) + \operatorname{div}\left(\rho\varepsilon\mathbf{v} + \tfrac{1}{2}\rho\mathbf{v}^2\mathbf{v} + p\mathbf{v} + \sigma\mathbf{v} + \mathbf{q}\right) &= 0, \end{aligned} \tag{4}$$

including the stress tensor σ and the heat flux $\mathbf{q}$. The R13 equations can be viewed as a generalized constitutive theory for stress tensor and heat flux. The standard local relations of NSF are extended to form full evolution equations for σ_{ij} and q_i. They are given by

$$\frac{\partial \sigma_{ij}}{\partial t} + \frac{\partial \sigma_{ij} v_k}{\partial x_k} + \frac{4}{5}\frac{\partial q_{\langle i}}{\partial x_{j\rangle}} + 2p\frac{\partial v_{\langle i}}{\partial x_{j\rangle}} + 2\sigma_{k\langle i}\frac{\partial v_{j\rangle}}{\partial x_k} + \frac{\partial m_{ijk}}{\partial x_k} = -\nu\,\sigma_{ij} \tag{5}$$

for the stress and

$$\begin{aligned}(6)\quad &\frac{\partial q_i}{\partial t}+\frac{\partial q_i v_k}{\partial x_k}+\frac{5}{2}p\frac{\partial \theta}{\partial x_i}+\frac{5}{2}\sigma_{ik}\frac{\partial \theta}{\partial x_k}+\theta\frac{\partial \sigma_{ik}}{\partial x_k}-\sigma_{ik}\frac{\theta}{\rho}\frac{\partial \varrho}{\partial x_k}-\frac{\sigma_{ij}}{\varrho}\frac{\partial \sigma_{jk}}{\partial x_k}\\ &\qquad+\frac{7}{5}q_k\frac{\partial v_i}{\partial x_k}+\frac{2}{5}q_k\frac{\partial v_k}{\partial x_i}+\frac{2}{5}q_i\frac{\partial v_k}{\partial x_k}+\frac{1}{2}\frac{\partial R_{ik}}{\partial x_k}+m_{ijk}\frac{\partial v_j}{\partial x_k}=-\frac{2}{3}\nu\, q_i\end{aligned}$$

for the heat flux. Both equations form quasi-linear first order equations with relaxation. The inverse relaxation time is given proportional to ν, the local mean collision frequency of the gas particles.

The remaining unspecified quantities are m_{ijk} and R_{ij}. They stem from higher moments contributions in the transfer equations of Boltzmann's equation. Neglecting these contributions turns the system (4)–(6) into the classical 13-moment case of Grad [15], [16]. In [40] gradient expressions are derived for m_{ijk} and R_{ij} which regularize Grad's equations and turn them into a highly accurate microflow model. While the original expressions in [40] contain nonlinear terms, in this paper we restrict ourselves to the linear parts given by

$$(7)\qquad m_{ijk}=-2\frac{\theta}{\nu}\frac{\partial \sigma_{\langle ij}}{\partial x_{k\rangle}},$$

$$(8)\qquad R_{ik}=-4\frac{\theta}{\nu}\left(\frac{\partial q_l}{\partial x_l}\delta_{ik}+\frac{6}{5}\frac{\partial q_{\langle i}}{\partial x_{k\rangle}}\right).$$

Equations (4)–(8) form the system of regularized 13-moment equations.

The evolution equations (5) and (6) for stress and heat flux are not in balance law form. Usually, the constitutive theory is more easily based directly on these primitive or internal variables. However, since the equations originated from transfer equations in balance law form, such a formulation can be found. We have

$$(9)\qquad \begin{aligned}&\frac{\partial}{\partial t}\rho+\frac{\partial}{\partial x_k}(\varrho v_k) &&=0,\\ &\frac{\partial}{\partial t}(\rho v_i)+\frac{\partial}{\partial x_k}\left(\rho v_i v_k+p_{ik}\right) &&=0,\\ &\frac{\partial}{\partial t}\left(p_{ij}+\rho v_i v_j\right)+\frac{\partial}{\partial x_k}\left(\rho v_i v_j v_k+3p_{(ij}v_{k)}+\tfrac{6}{5}\delta_{(ij}q_{k)}+m_{ijk}\right) &&=-\nu\, p_{\langle ij\rangle},\\ &\frac{\partial}{\partial t}\left(2q_i+2p_{ij}v_j+3pv_i+\rho v_i v_j^2\right)\\ &\quad+\frac{\partial}{\partial x_k}\Big(\tfrac{28}{5}q_{(i}v_{k)}+p_{ik}\left(7\theta+v_j^2\right)+\left(3p+\rho v_j^2\right)v_i v_k\\ &\qquad+4v_j p_{j(i}v_{k)}+2\left(\tfrac{2}{5}\delta_{ik}q_j+m_{ikj}\right)v_j-2\theta p\delta_{ik}+R_{ik}\Big) &&=-2\nu(p_{\langle ij\rangle}v_j+\tfrac{2}{3}\,q_i)\end{aligned}$$

as the R13 system equivalent to (4)–(6). Here the evolved quantities are the so-called convective moments. In this formulation it turned out to be more natural to use the pressure tensor p_{ij} as variable. Hence, the energy equation and the equation for the stress tensor are merged into a single row in (9). The energy equation may be recovered by taking the trace of this row. Apparently, this is the first time that Grad's 13-moment equations are explicitly given in full three-dimensional balance law formulation in the literature.

The system (9) has the form

$$\partial_t U + \operatorname{div} \mathbf{F}(U) = P(U) \tag{10}$$

with a flux function $\mathbf{F}$ and a relaxational source P. In the regularized case $\mathbf{F}$ contains diffusive gradient terms. The convective variables are called

$$U = \{\rho, M_i, P_{ij}, Q_i\}, \tag{11}$$

and the flux function may be split into the three directions and four convective variables

$$\mathbf{F}(U) = \begin{pmatrix} F^{(\rho),x} & F^{(\rho),y} & F^{(\rho),z} \\ F_i^{(M),x} & F_i^{(M),y} & F_i^{(M),z} \\ F_{ij}^{(P),x} & F_{ij}^{(P),y} & F_{ij}^{(P),z} \\ F_i^{(Q),x} & F_i^{(Q),y} & F_i^{(Q),z} \end{pmatrix}. \tag{12}$$

We note that the knowledge or implementation of the flux in a single direction suffices to calculate the flux in any direction. This is due to Galilean invariance. If the flux is required in the direction of the vector $\mathbf{n}$, all quantities have to be rotated into this direction. The general procedure is given by

$$\mathbf{F}(U)\cdot\mathbf{n} = \begin{pmatrix} F^{(\rho),x}(\rho, M_j\mathcal{R}_{ji}, P_{kl}\mathcal{R}_{ki}\mathcal{R}_{lj}, Q_j\mathcal{R}_{ji}) \\ \mathcal{R}_{ij}F_j^{(M),x}(\rho, M_j\mathcal{R}_{ji}, P_{kl}\mathcal{R}_{ki}\mathcal{R}_{lj}, Q_j\mathcal{R}_{ji}) \\ \mathcal{R}_{ik}\mathcal{R}_{jl}F_{kl}^{(P),x}(\rho, M_j\mathcal{R}_{ji}, P_{kl}\mathcal{R}_{ki}\mathcal{R}_{lj}, Q_j\mathcal{R}_{ji}) \\ \mathcal{R}_{ij}F_j^{(Q),x}(\rho, M_j\mathcal{R}_{ji}, P_{kl}\mathcal{R}_{ki}\mathcal{R}_{lj}, Q_j\mathcal{R}_{ji}) \end{pmatrix} \tag{13}$$

with the rotation matrix $\mathcal{R}_{ij}$ based on the direction $\mathbf{n}$. This is equivalent to the property of the Euler equations where the y-flux follows from the x-flux after substituting the velocity vector $(v_x, v_y) \to (v_y, -v_x)$. In the present case the structure is more involved due to higher tensorial degrees.

3.2. Relation to Boltzmann's equation and NSF. We will briefly discuss how to relate the R13 system to standard models and Boltzmann's equation. Most of this discussion was done in detail in [40] and [44] based on asymptotic analysis.

The mean collision frequency is given by ν and appears in the right-hand side of the R13 equations. Introducing the mean free path at a reference state by

$$\lambda_0 = \frac{\sqrt{\theta_0}}{\nu_0} \tag{14}$$

we have the fundamental microscopic length scale. Macroscopic length and time scales are fixed such that

$$L/T = \sqrt{\theta_0}, \tag{15}$$

where $\sqrt{\theta_0}$ represents the isothermal equilibrium speed of sound. It is considered as the velocity scale in the system. Note that all moments can be scaled by a reference density ρ_0 and appropriate powers of $\sqrt{\theta_0}$. The Knudsen number is defined by

$$Kn = \frac{\lambda_0}{L} = \frac{1}{\nu_0 T} \tag{16}$$

and appears as factor $1/Kn$ in the right-hand side of the dimensionless equations.

In those applications we have in mind that the Knudsen number is a small number, $Kn < 1$. Hence, an asymptotic expansion in powers of Kn is reasonable. In the spirit of a Chapman–Enskog expansion we write

$$\sigma_{ij} = \sigma_{ij}^{(0)} + Kn\,\sigma_{ij}^{(1)} + Kn^2\,\sigma_{ij}^{(2)} + \ldots, \tag{17}$$

$$q_i = q_i^{(0)} + Kn\,q_i^{(1)} + Kn^2\,q_i^{(2)} + \ldots \tag{18}$$

for the stress tensor and heat flux. This expansion can now be introduced into the full Boltzmann equation; see [11], [46], or any continuum model, such as the R13 system (4)–(8). In general, the result will differ at a certain stage of the expansion. Assuming the validity of Boltzmann's equation, we define this difference as a measure for the accuracy of the continuum model.

In [44] it was shown that Chapman–Enskog expansion of the R13 system leads to the result of Boltzmann's equation *up to third order in* Kn at least for the case of Maxwell molecules. This means that any R13 result will differ from a full Boltzmann simulation only in $\mathcal{O}\left(Kn^4\right)$. Thus, for asymptotic reasons the system is the most accurate stable continuum model currently available.

The first order of the expansion gives the relations of NSF of compressible gas dynamics for both the Boltzmann equation and the R13 system. The expressions are given by

$$\sigma_{ij}^{(1)} = -2\frac{p}{\nu}\frac{\partial v_{\langle i}}{\partial x_{j\rangle}} \quad \text{and} \quad q_i^{(1)} = -\frac{15}{4}\frac{p}{\nu}\frac{\partial \theta}{\partial x_i}. \tag{19}$$

This shows that for very small Knudsen numbers the R13 system will essentially behave like the NSF equations. From (19) we can identify the transport coefficients and relate them to the mean collision frequency in order to have a practical expression for ν. Usually the viscosity is given by

$$\mu = \mu_0 \left(\frac{\theta}{\theta_0}\right)^s \tag{20}$$

with a temperature exponent $0.5 \leq s \leq 1$. Hence, we will use

$$\nu = \frac{\theta_0^s}{\mu_0}\,\rho\,\theta^{1-s} \tag{21}$$

for the collision frequency which leads to asymptotically correct transport coefficients. Sometimes it is asked what the transport coefficients are used for in the R13 system. However, the term "transport coefficients," i.e., coefficients in (19), is not defined for the system, since the relations (19) are entirely substituted by the evolution equations (5) and (6).

The definition of the collision frequency leads to the expression

$$\lambda_0 = \frac{\mu_0}{\rho_0\sqrt{\theta_0}} \tag{22}$$

for the mean free path. This differs from a standard value

$$\bar{\lambda}_0 = \frac{4}{5}\frac{\mu_0}{\rho_0\sqrt{\frac{\pi}{8}\theta_0}} \tag{23}$$

given, e.g., in [11] by a factor of $\frac{4}{5}\sqrt{\frac{8}{\pi}} \approx 1.28$. The definition (14) is used to avoid additional factors in the dimensionless equations.

3.3. Two-dimensional equations. This paper will set up numerical methods for the R13 system in two dimensions. In two dimensions we consider the reduced variables in the notation

$$v_i = (v_x, v_y, 0)\,, \quad p_{ij} = \begin{pmatrix} p_x & p_{xy} & 0 \\ p_{xy} & p_y & 0 \\ 0 & 0 & p_z \end{pmatrix}, \quad q_i = (q_x, q_y, 0) \tag{24}$$

and assume homogeneity in the z-direction. Note that while the shear stresses p_{xz} and p_{yz} vanish, the diagonal element p_z might be different from zero. This follows from the kinetic definition of $p_z = \int C_z^2 f\, d\mathbf{C}$. In the z-direction the distribution function is assumed to be isotropic, but it my deviate (isotropically) from its equilibrium value. Hence, all even moments such as p_z will have a nonequilibrium value.

Instead of the directional pressures p_x, p_y, and p_z we will consider p_x, p_y, and the full pressure

$$p = \frac{1}{3}\left(p_x + p_y + p_z\right) \tag{25}$$

as basis variables. The single shear stress will be denoted by $\sigma := \sigma_{xy} = p_{xy}$. Together with the density we have nine independent variables for the two-dimensional R13 equations given by

$$W = \left\{\rho, v_x, v_y, p, p_x, p_y, \sigma, q_x, q_y\right\}. \tag{26}$$

In the following the abbreviation $v^2 = v_x^2 + v_y^2$ for the square of the velocity vector is used. In one-dimensional calculations the set of variables is further reduced. We have $v_y = q_y = p_{xy} = 0$ and $p_y = p_z$; hence five variables $\{\rho, v_x, p, p_x, q_x\}$ remain. In what follows we will occasionally consider the full two-dimensional variable set but restrict the spatial dependence to one dimension. This is sometimes called 1.5 dimensional.

As shown above the equations can be written in the balance law form

$$\partial_t U\left(W\right) + \operatorname{div} \mathbf{F}(W) = P(W). \tag{27}$$

Here the two-dimensional divergence $\operatorname{div} = (\partial_x, \partial_y)$ is used and the flux function is split into $\mathbf{F}\left(W\right) = \left(F\left(W\right), G\left(W\right)\right)$. Since the tensorial notation in (9) does not provide an easy detailed insight into the explicit equations we proceed with giving explicit functions for U, F, G, and P written in the variables (26). The convective moments are given by

$$U\left(W\right) = \begin{pmatrix} \rho \\ \rho v_x \\ \rho v_y \\ \rho v^2 + 3p \\ \rho v_x^2 + p_x \\ \rho v_y^2 + p_y \\ \rho v_x v_y + \sigma \\ \rho v_x v^2 + 3p v_x + 2\left(p_x v_x + \sigma v_y\right) + 2q_x \\ \rho v_y v^2 + 3p v_y + 2\left(p_y v_y + \sigma v_x\right) + 2q_y \end{pmatrix}, \tag{28}$$

while the flux functions are

(29)
$$F(W) = \begin{pmatrix} \rho v_x \\ \rho v_x^2 + p_x \\ \rho v_x v_y + \sigma \\ \rho v_x v^2 + 2\left(p_x v_x + \sigma v_y\right) + 3p v_x + 2q_x \\ \rho v_x^3 + 3p_x v_x + \frac{6}{5} q_x + m_{xxx} \\ \rho v_x v_y^2 + p_y v_x + 2\sigma v_y + \frac{2}{5} q_x + m_{xyy} \\ \rho v_y v_x^2 + p_x v_y + 2\sigma v_x + \frac{2}{5} q_y + m_{xxy} \\ \left(\rho v^2 + 3p + 4p_x\right) v_x^2 + \left(7\theta + v^2\right) p_x + 4\sigma v_x v_y + \frac{32}{5} q_x v_x + \frac{4}{5} q_y v_y - 2\theta p + \hat{R}_{xx} \\ \left(\rho v^2 + 3p + 2\left(p_x + p_y\right)\right) v_x v_y + \left(7\theta + 3v^2\right)\sigma + \frac{14}{5}\left(q_x v_y + q_x v_y\right) + \hat{R}_{xy} \end{pmatrix}$$

in the x-direction and

(30)
$$G(W) = \begin{pmatrix} \rho v_y \\ \rho v_x v_y + \sigma \\ \rho v_y^2 + p_y \\ \rho v_y v^2 + 2\left(p_y v_y + \sigma v_x\right) + 3p v_y + 2q_y \\ \rho v_y v_x^2 + p_x v_y + 2\sigma v_x + \frac{2}{5} q_x + m_{yxx} \\ \rho v_y^3 + 3p_y v_y + \frac{6}{5} q_y + m_{yyy} \\ \rho v_x v_y^2 + p_y v_x + 2\sigma v_y + \frac{2}{5} q_y + m_{xyy} \\ \left(\rho v^2 + 3p + 2\left(p_x + p_y\right)\right) v_x v_y + \left(7\theta + 3v^2\right)\sigma + \frac{14}{5}\left(q_x v_y + q_x v_y\right) + \hat{R}_{xy} \\ \left(\rho v^2 + 3p + 4p_y\right) v_y^2 + \left(7\theta + v^2\right) p_y + 4\sigma v_x v_y + \frac{32}{5} q_y v_y + \frac{4}{5} q_x v_x - 2\theta p + \hat{R}_{yy} \end{pmatrix}$$

in the y-direction. A detailed inspection shows the strong structural relation between F and G.

The fluxes require the values of m_{ijk} and $\hat{R}_{ij} = m_{ijk} v_k + R_{ij}$. Using tensorial identities the expressions (7) and (8) give in explicit two-dimensional notation

(31)
$$\begin{pmatrix} m_{xxx} \\ m_{xxy} \\ m_{xyy} \\ m_{yyy} \end{pmatrix} = -2\frac{\theta}{\nu} \begin{pmatrix} \frac{3}{5}\left(\partial_x p_x - \partial_x p\right) - \frac{2}{5}\partial_y \sigma \\ \frac{1}{3}\partial_y p_x - \frac{1}{5}\partial_y p + \frac{8}{15}\partial_x \sigma - \frac{2}{15}\partial_y p_y \\ \frac{1}{3}\partial_x p_y - \frac{1}{5}\partial_x p + \frac{8}{15}\partial_y \sigma - \frac{2}{15}\partial_x p_x \\ \frac{3}{5}\left(\partial_y p_y - \partial_y p\right) - \frac{2}{5}\partial_x \sigma \end{pmatrix}$$

and

(32)
$$\begin{pmatrix} R_{xx} \\ R_{xy} \\ R_{yy} \end{pmatrix} = -4\frac{\theta}{\nu} \begin{pmatrix} \frac{5}{3}\partial_x q_x + \frac{2}{3}\partial_y q_y \\ \frac{1}{2}\left(\partial_x q_y + \partial_y q_x\right) \\ \frac{5}{3}\partial_y q_y + \frac{2}{3}\partial_x q_x \end{pmatrix},$$

which can be directly utilized in the flux functions. In the cases $m_{ijk} = 0$ and $R_{ij} = 0$ the flux functions reduce to the nonregularized fluxes, called $F^{(0)}(W)$ and $G^{(0)}(W)$. These correspond to Grad's 13-moment case in two dimensions.

Finally, the relaxational source is given by

$$P(W) = \begin{pmatrix} \mathbf{0} \in \mathbb{R}^4 \\ -\nu(p_x - p) \\ -\nu(p_y - p) \\ -\nu\sigma \\ -2\nu\left(\sigma v_y + (p_x - p)v_x + \frac{2}{3}q_x\right) \\ -2\nu\left(\sigma v_x + (p_y - p)v_y + \frac{2}{3}q_y\right) \end{pmatrix}, \tag{33}$$

which completes the system (27).

3.4. Directional temperatures. Directional temperatures are derived by integration of the distribution function multiplied by parts of the square of C_i, i.e., C_x^2, C_y^2, and C_z^2. These integrals are part of the variable vector of the R13 system in the form of the directional pressures $p_{x,y,z}$ given by

$$p_{x,y,z} = m\int_{\mathbb{R}^3} C_{x,y,z}^2 f\, d\mathbf{C}. \tag{34}$$

The directional temperatures in energy units are defined by

$$p_x = \rho\theta_x, \quad p_y = \rho\theta_y, \quad p_z = \rho\theta_z \tag{35}$$

and are related to the full temperature by $\theta = \frac{1}{3}(\theta_x + \theta_y + \theta_z)$. A directional temperature model for shock waves was also considered, e.g., in [10]. If the directional temperatures are scaled by $\hat{\theta}_x = \theta_x/\theta$, it follows that the constraint

$$0 < \hat{\theta}_p < \hat{\theta}_p + \hat{\theta}_q < 3 \tag{36}$$

for $p, q \in \{x, y, z\}$ and $p \neq q$. In equilibrium we have $\hat{\theta}_x = \hat{\theta}_y = \hat{\theta}_z = 1$.

We conclude that the set of variables of the R13 system in two space dimensions consists of the equilibrium variables density, velocity, and full temperature and the nonequilibrium variables x- and y-temperature, x- and y-heat flux, and the shear stress.

Note that the normal stresses are given by

$$\sigma_{xx} = \rho(\theta_x - \theta), \quad \sigma_{yy} = \rho(\theta_y - \theta), \quad \sigma_{zz} = \rho(\theta_z - \theta). \tag{37}$$

Using the Navier–Stokes relation (19) the directional temperatures can be calculated for any NSF simulation.

3.5. Speed of propagation. The homogeneous, nonregularized system

$$\partial_t U(W) + \operatorname{div}\mathbf{F}^{(0)}(W) = 0 \tag{38}$$

with vanishing productions and $m_{ijk} = R_{ij} = 0$ forms a hyperbolic system of conservation laws. The propagation speeds in the one-dimensional case were studied in the

textbook [29]. The two-dimensional equilibrium case is sketched by Grad in [16]. The fastest propagation speed will be important in the numerical method below.

After differentiation and restriction to one dimension the system can be written in the form

$$\partial_t W + A\,\partial_x W = 0 \tag{39}$$

with the 9×9 matrix

$$A = \begin{pmatrix}
v_x & \rho & 0 & 0 & 0 & 0 & 0 & 0 & 0 \\
0 & v_x & 0 & 0 & \frac{1}{\rho} & 0 & 0 & 0 & 0 \\
0 & 0 & v_x & 0 & 0 & 0 & \frac{1}{\rho} & 0 & 0 \\
0 & p + \frac{2}{3}p_x & \frac{2}{3}\sigma & v_x & 0 & 0 & 0 & \frac{2}{3} & 0 \\
0 & 3p_x & 0 & 0 & v_x & 0 & 0 & \frac{6}{5} & 0 \\
0 & p_x & 2\sigma & 0 & 0 & v_x & 0 & \frac{2}{5} & 0 \\
0 & 2\sigma & p_y & 0 & 0 & 0 & v_x & 0 & \frac{2}{5} \\
\frac{p(2p-7p_x)}{2\rho^2} & \frac{16}{5}q_x & 0 & \frac{7p_x-4p}{2\rho} & \frac{2p-p_x}{\rho} & 0 & -\frac{\sigma}{\rho} & v_x & 0 \\
-\frac{7p\sigma}{2\rho^2} & \frac{7}{5}q_y & \frac{7}{5}q_x & \frac{7\sigma}{2\rho} & -\frac{\sigma}{\rho} & 0 & \frac{2p-p_x}{\rho} & 0 & v_x
\end{pmatrix}. \tag{40}$$

The propagation speeds are given by the eigenvalues of A which have the form

$$\lambda_j = v_x + c_j \left(\frac{p_x}{p}, \frac{p_y}{p}, \frac{\sigma}{p}, \frac{q_x}{p\sqrt{\theta}}, \frac{q_y}{p\sqrt{\theta}} \right) \sqrt{\theta}, \qquad j = 1, 2, \ldots, 9, \tag{41}$$

but cannot be derived explicitly in general. In "equilibrium," i.e., $\sigma = q_x = q_y = 0$ and $p_x = p_y = p$, the values of c_j are given in the form of multiple roots. They evaluate to be

$$\{c_j\}_{j=1,2,\ldots,8} = \{0, 0, \pm 0.812, \pm 1.183, \pm 2.130\}\,. \tag{42}$$

Especially the largest value takes the form

$$c_{\max}^{(0)} = 2.130\sqrt{\theta} = 1.65\sqrt{5/3\,\theta}; \tag{43}$$

hence the propagation speed is 1.65 times the adiabatic sound speed, a value already given by Grad [15].

There exists some confusion about the relevance of the characteristic speeds (42), especially in comparison with the speeds of the Euler equations given by $v_x \pm \sqrt{5/3\,\theta}$ and v_x for a monatomic gas. However, to some extent this comparison is misleading. The homogeneous system (38) must be considered as an approximation to the Boltzmann equation in the case of the vanishing right-hand side, i.e., $Kn \to \infty$. In that sense the free-flight equation $\partial_t f + c_i \partial_i f = 0$ is substituted by the hyperbolic continuum model (38). In this model the particle propagation with real-valued velocity is represented by discrete modes given by the characteristic speeds. The distribution function is replaced by Dirac deltas placed at velocity values given by λ_j with factors such that the original distribution function is approximated. In the absence of stress and heat flux these velocity values are specific modes given by (42) which are

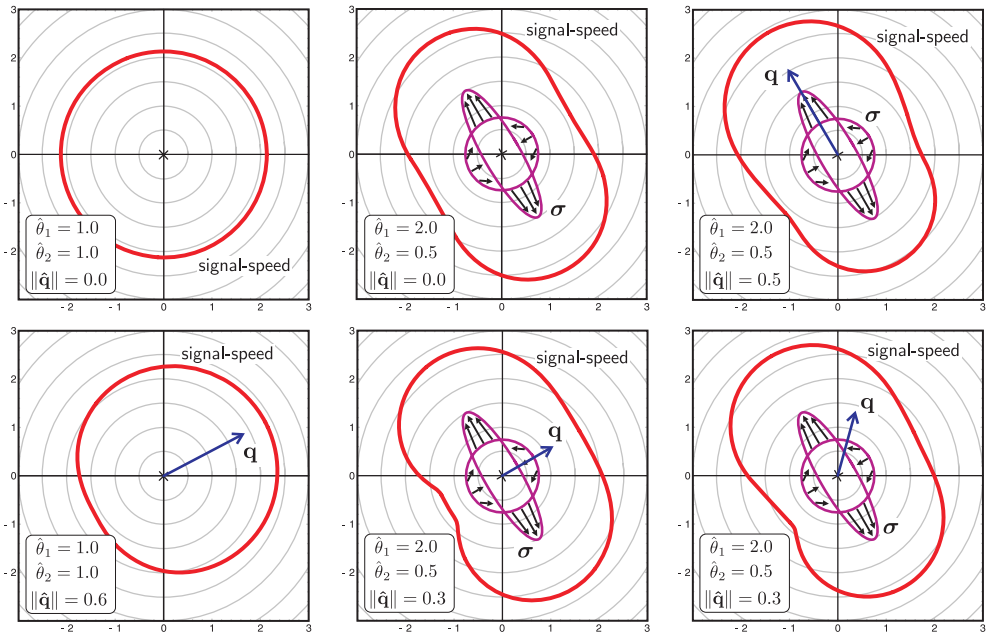

FIG. 1. *Two-dimensional maximal signal speed for the homogeneous Grad's* 13*-moment system. Different nonequilibrium states distort the signal speed similar to the shape of a corresponding distribution function.*

more or less arbitrary and solely introduced by a certain choice of a finite number of continuum variables [29].

In view of this discussion we investigate the value of the fastest propagation speed for different values of directional temperatures, shear stress, and heat flux. In nonequilibrium the distribution function deviates from the isotropic Maxwellian. Different directional temperatures introduce an ellipsoidal shape, and the heat flux specifies a preferred direction. The propagation speed of the homogeneous system (38) mimics this behavior.

Figure 1 gives some snapshots of the two-dimensional signal speeds arising from different nonequilibrium situations. Note that the speed in a certain direction $\mathbf{n}$ can be calculated from the one-dimensional result (41) by rotating the values of heat flux and pressure tensor into the required direction as in (13). The plots in the figure are Friedrichs diagrams in which the fastest signal mode is displayed as parametric curve $c_{\max}(\mathbf{n})\,\mathbf{n}$. The line represents a wave front after one time unit started as a point from the origin. Additionally, in each plot the shape of the stress tensor is sketched as its action to a circular volume. The direction of the heat flux is shown as an arrow. The directional temperatures $\hat{\theta}_1$ and $\hat{\theta}_2$ are calculated in the directions of the eigenvectors of the stress tensor.

The upper left plot shows the isotropic equilibrium situation, the upper middle plot the presence of stress with no heat flux, and the lower left plot the presence of a heat flux with no stress. The remaining three plots display the interaction between stress and heat flux in different directions. The figure demonstrates the ability of the homogeneous system to approximate the principal shape of the underlying velocity distribution function.

From this point of view the characteristic speeds (42) approximate the information

transport in a noncollisional, free-flight gas with vanishing stress and heat flux. In contrast, the Euler equations represent the case $Kn \to 0$ and the Euler speeds the propagation of sound waves in an equilibrium gas where collisions are dominant. Such sound waves can be obtained from the R13 system as well when relaxation and dissipation are included; see [40].

It is known that the expression (41) will not yield real values for all nonequilibrium states; see [29] or [43]. Indeed, only in some vicinity of equilibrium can this be assured. This means the homogeneous system is hyperbolic only in a specific domain of hyperbolicity. Loss of hyperbolicity is often brought forward as an objection against the usefulness of, e.g., Grad's equations. However, there is an important issue that refutes this objection. The loss occurs only at a very high level of nonequilibrium represented by large Knudsen numbers. At this level, the equations are not valid because of their derivation as a model for moderate Knudsen numbers. This statement can be quantitized. The analysis of hyperbolicity shows that $p_{x,y}/p \gtrsim 0.2$, and $\left\|q_i/(p\sqrt{\theta})\right\| \lesssim 0.6$ leads to loss of hyperbolicity of the 13-moment case; see [29]. To evaluate these conditions we consider the NSF relations (19) as approximation to σ_{ij} and q_i and deduct conditions on the relative change in velocity and temperature. We find that

$$\frac{\Delta v/\sqrt{\theta}}{\Delta x/\lambda} \lesssim 40\% \quad \text{and} \quad \frac{\Delta \theta/\theta}{\Delta x/\lambda} \lesssim 16\%; \tag{44}$$

i.e., relative change in velocity and temperature over a *single mean free path* is restricted to be below 40% and 16%, respectively. This conditions state a strong nonequilibrium at which the validity of the continuum model is no longer assured. In any reasonable simulation based on the 13-moment equation such a nonequilibrium should be avoided. Accordingly, the results in this paper stay below these values.

All this is valid for the homogeneous system without productions and higher order contributions. In the calculations the interaction of the relaxation and dissipation with the hyperbolic waves will lead to damped and smooth solutions. A linear analysis has shown that all waves in the full regularized 13-moment system are entirely stable for all wavelengths and frequencies; see [40]. Because of the interaction with relaxation and dissipation the hyperbolic waves are less dominant in the solution than the hyperbolic waves in the case of the Euler equations.

Due to initial layers occasional violations of hyperbolicity cannot be entirely ruled out in a numerical simulation. Experience shows that these violations due to occasional high nonequilibrium are usually quickly cured by damping and smoothing effects in the system. However, a numerical method should be robust enough to handle such a violation. Numerical evaluation of the eigenvalue shows that, even though some values turn complex, there will always be a direction with a fastest speed that is real. A wave front with partial loss of hyperbolicity is given in Figure 2. The front is torn apart, but the general shape is still clearly visible. In particular, a maximal wave speed can be defined.

4. Numerical method.

This section will provide a robust and accurate numerical method for the R13 system in two dimensions as given in (27)–(33).

4.1. Numerical approaches.

The system to solve can be written in the form

$$\partial_t U + \operatorname{div} \mathbf{F}^{(0)}(U) = P(U) + \operatorname{div}\left(\mathbf{D}(U) \cdot \operatorname{grad} U\right) \tag{45}$$

with a hyperbolic flux $\mathbf{F}^{(0)} : \mathbb{R}^N \to \mathbb{R}^{N\times d}$, a relaxational source $P : \mathbb{R}^N \to \mathbb{R}^N$, and a dissipative second order term with a coefficient matrix $\mathbf{D} : \mathbb{R}^N \to \mathbb{R}^{(N\times d)\times(N\times d)}$. The

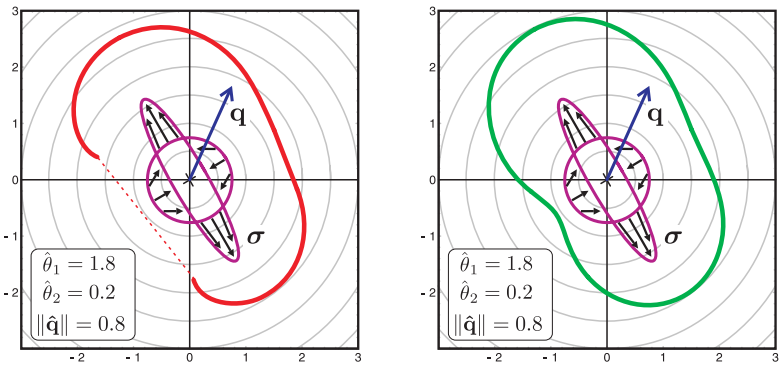

FIG. 2. *Left: fastest wave front of the homogeneous system with loss of hyperbolicity along the dashed line in the case of strong nonequilibrium. Right: the same situation but with the approximate wave front obtained from the approximation* (50).

system is quasi-linear of hyperbolic-parabolic type. Apart from the relaxational source the structure is the same as for the system of NSF for compressible gas dynamics. The full flux is denoted by

$$\mathbf{F}\left(U, \operatorname{grad} U\right) = \mathbf{F}^{(0)}\left(U\right) + \mathbf{D}(U) \cdot \operatorname{grad} U \tag{46}$$

for convenience.

A standard approach for a numerical method would be to split the actual evolution operator into the hyperbolic, parabolic, and relaxational operator and solve each part successively within a fractional step method. Each part could be discretized in an optimal way using an accurate method specified for the actual type of operator. However, as mentioned above, the interplay of the different parts of the evolution equation, i.e., transport, relaxation, and dissipation, constitutes the essential feature of the solution behavior. Thus, a fully split method could miss the actual physics of the system.

Numerical methods for hyperbolic conservation laws with relaxation are studied in several papers. Typical equations considered are the Broadwell model in kinetic theory or a 2×2 relaxational extension of a scalar conservation law. Grad's 13-moment system falls into the same class of equations. For the limit of small relaxational times these equations reduce to an equilibrium system. In [17] Jin investigates a splitting procedure which duplicates the analytical behavior into a stable and efficient asymptotic preserving numerical method. This approach is refined and extended, e.g., in the works [9] by Caflisch, Jin, and Russo and [32] by Pareschi and Russo. Liotta, Romano, and Russo in [27] solved Grad's 13-moment equation in the equilibrium limit with such an approach. The equilibrium system of the R13 equations is the Euler equations, since for $Kn \to 0$ stress and heat flux vanish. For nonvanishing Knudsen numbers stress and heat flux are nonzero, and the production terms are interacting with the fluxes, creating a nonequilibrium solution. In this range the numerical approach of well-balanced schemes as described by LeVeque in [25] might be useful, especially in stationary solutions. For larger Knudsen numbers and finer grids the parabolic part in the system introduces an additional stiffness. Explicit methods which are simple to implement can be stabilized by using adaptive many-stage Runge–Kutta methods as described, e.g., in [1] by Abdulle and Medovikov.

The simulations of the R13 system in this paper will focus on the range $0.01 \leq$

$Kn \leq 1.0$ and instationary solutions in two dimensions. So far, numerical solutions in this setting have never been calculated. Even though an asymptotic preserving and well-balanced scheme would be preferable, this paper will start with a standard explicit finite volume method for (45) extended by the relaxational and dissipative parts in a straightforward way. These extensions are stabilized to a sufficient amount resulting in a robust and simple method for instationary R13 simulations at moderate Knudsen numbers. The enhancement of the numerical method is left for future work.

4.2. Homogeneous hyperbolic system. We assume a finite volume discretization based on rectangular grid cells with cell centers (x_i, y_i) and mean cell values $U^n_{i,j}$ at time level n. The extension of the method to triangular grids is straightforward. The main ingredients of the method are derived for the one-dimensional case and extended to two dimensions afterwards.

4.2.1. Second order Harten–Lax–van Leer (HLL) flux. We consider the homogeneous hyperbolic system of the R13 equations; i.e., we neglect the source P and the gradient terms in the flux. The numerical method is based on a HLL flux [12] with a linear reconstruction and second order time integration; see [14] or [24].

The update itself is performed for the convective variables U, especially the conservative variables density, momentum density, and total energy density. However, it is recommended to conduct the calculations of each time step of the method in primitive variables W. We have $W_i = W(U_i)$ for each cell. The update $\mathcal{H}(W^n, \Delta t)$ for U^n_i uses the conservative intercell flux formulation

$$\mathcal{H}(W^n, \Delta t)|_i := U(W^n_i) + \frac{\Delta t}{\Delta x}\left(\tilde{F}^{HLL}_{i-\frac{1}{2}} - \tilde{F}^{HLL}_{i+\frac{1}{2}}\right) \tag{47}$$

based on a standard HLL flux as given in Appendix A.

The update is used in the Heun method for time integration

$$\begin{aligned} U^{(1)} &= \mathcal{H}(W(U^n), \Delta t), \\ U^{n+1} &= \frac{1}{2}\left(U^n + \mathcal{H}\left(W\left(U^{(1)}\right), \Delta t\right)\right) \end{aligned} \tag{48}$$

using a temporary variable $U^{(1)}$ and two full time step evaluations. For the homogeneous system this yields second order in space and time. Several other possible second order time integrations exist. Heun's method has a simple structure using two full time step evaluations. It also provides TVD properties in the context of scalar conservation laws. The procedure (48) is the building block of our method for the solution of the R13 equations. Relaxation and dissipation will now be incorporated directly into the update (47) in an efficient and practical way.

The time step in (47) has to be chosen according to the stability condition

$$\frac{\lambda_{\max}\Delta t}{\Delta x} \leq 1, \tag{49}$$

where $\lambda_{\max} = \max(v_x \pm c_{\max})$ is the maximal characteristic speed following from the maximal signal speed $c_{\max}$.

4.2.2. Speed approximation. The calculation of the exact eigenvalues of the matrix (40) to obtain $c_{\max}$ is numerically expensive and lacks robustness due to the occasional risk of existence of complex eigenvalues. We discuss two cheaper approximations for the calculation of $c_{\max}$.

A detailed investigation of the eigenvalues and an empirical adjustment resulted in a useful approximation of $c_{\max}$ given by

$$\frac{c_{\max}(\mathbf{n})}{\sqrt{\theta}} \approx c^{(p)}(P_2) + \left(c^{(p)}(P_1) - c^{(p)}(P_2)\right)\mathbf{n}\cdot\mathbf{r}_1 + c^{(q)}\left(\frac{\|\mathbf{q}\|}{\rho\sqrt{\theta}^3}\right)\frac{\mathbf{n}\cdot\mathbf{q}}{\|\mathbf{q}\|} \tag{50}$$

depending on the stress and heat flux. The values $P_{1,2}$ are the dimensionless eigenvalues of the normalized two-dimensional pressure deviator

$$\hat{p}_{ij} = \begin{pmatrix} p_x/p & \sigma/p \\ \sigma/p & p_y/p \end{pmatrix}. \tag{51}$$

The vector $\mathbf{r}_1$ is the eigenvector corresponding to P_1. The functions $c^{(p)}$ and $c^{(q)}$ calculate the maximal signal speed based on the presence of only stress or only heat flux. Again, based on empirical adjustments approximate expressions for these functions are found to be

$$c^{(p)}(P) = c^{(0)}_{\max}/\sqrt{\theta} - 0.9 + P - 0.1P^2 \tag{52}$$

and

$$c^{(q)}(Q) = \sqrt[4]{(c^{(0)}_{\max}/\sqrt{\theta})^4 + 25Q} - c^{(0)}_{\max}/\sqrt{\theta}. \tag{53}$$

The approximation (50) is capable of describing the general shape of the two-dimensional signal speed as in Figure 1. An example is given in the right-hand side of Figure 2.

In contrast to the case of Euler equations, the nonconvective characteristic speed c_j in the present case is direction dependent. For the calculation of an intercell flux between two states $W_{L,R}$ we define

$$c^R_{\max} = \left|c_{\max}\left((1,0)^T; W^{(R)}\right)\right|, \qquad c^L_{\max} = \left|c_{\max}\left((-1,0)^T; W^{(L)}\right)\right| \tag{54}$$

as the maximal value to the right and to the left. These values enter the calculation of the numerical flux above.

Vector iteration. If the maximal eigenvalue is real, vector iteration is a suitable method since the value is needed only approximately. We briefly discuss a variant of the method adopted to the current problem. This represents an alternative method to calculate $c_{\max}$.

In many cases, e.g., in equilibrium, the matrix A in (40) has a maximal eigenvalue λ_1 and a minimal eigenvalue $\lambda_2 = -\lambda_1$. In such a case standard vector iteration does not converge. The squared method given by

$$\mathbf{V}^{(k+1)} = A^2\mathbf{V}^{(k)}, \qquad \lambda^{(k)} = \sqrt{\frac{\left\|\mathbf{V}^{(k+1)}\right\|}{\left\|\mathbf{V}^{(k)}\right\|}} \tag{55}$$

for $k = 1, 2, \ldots$ starting from some initial vector $V^{(0)}$ converges in the sense $\lim_{k\to\infty}\lambda^{(k)} = |\lambda_1| = |\lambda_2|$. This can be seen by considering the initial decomposition $\mathbf{V}^{(0)} = \sum_{j=1}^{N}\mathbf{r}_j$ of $V^{(0)}$ into eigenvectors $\mathbf{r}_j$ of A. In the special case $\lambda_2 = -\lambda_1$ and $|\lambda_j| < |\lambda_1|$ for $j > 2$ we have

$$\mathbf{V}^{(k)} = \sum_{j=1}^{N}\lambda_j^{2k}\mathbf{r}_j = \lambda_1^{2k}(\mathbf{r}_1 + \mathbf{r}_2) + \sum_{j=3}^{N}\left(\frac{\lambda_j}{\lambda_1}\right)^{2k}\mathbf{r}_j \tag{56}$$

and thus

$$\lambda^{(k)} = |\lambda_1| + \sum_{j=3}^{N} \mathcal{O}\left(\left(\frac{\lambda_j}{\lambda_1}\right)^{2k}\right). \tag{57}$$

The analogous result follows for regular case $|\lambda_2| < |\lambda_1|$.

Since the eigenvalues are expected to differ only slightly between computational grid cells the method converges fast if the current iteration vector $V^{(k)}$ is saved for the neighboring cell. In such an implementation the maximal eigenvalue is found in one or two iterations up to 5% error in most cases. However, this method fails if the largest value for $|\lambda_j|$ is based on a complex eigenvalue since its complex conjugated counterpart spoils the convergence. This is the case for strongly disparate values of θ_x and θ_y and $\hat{\theta}_x \lesssim 0.2$ and vanishing heat flux. Furthermore, the method yields only the maximal spectral radius and not direction dependent values as above.

4.3. Relaxational source. The relaxational right-hand side of the R13 system possesses a linear structure and leads to an exponential decay of stress and heat flux with a time scale proportional to Kn^{-1} in dimensionless formulations. To avoid strong time step restrictions and provide the correct asymptotics special treatment is necessary in some cases; see section 4.1. Here we present a simple extension of the Heun method based on the linear structure of the relaxation. The stabilization and accuracy will be sufficient for the applications with a moderate Knudsen number.

In the spatially homogeneous case the equations for stress (5) and heat flux (6) have the form

$$\partial_t \sigma_{ij} = -\nu\, \sigma_{ij} \quad \text{and} \quad \partial_t q_i = -\frac{2}{3}\nu\, q_i, \tag{58}$$

which show exponential solutions for constant ν. In order to incorporate this knowledge into the second order Heun update (48) in a stable way we first consider a model in the form of the scalar damped advection equation

$$\partial_t u + a\partial_x u = -\nu u \tag{59}$$

with $a, \nu > 0$ as the model for the Grad's 13-moment system. We propose

$$u_i^{(1)} = R\left(\nu\Delta t\right) u_i^n + \frac{a\Delta t}{\Delta x}\left(u_{i-1}^n - u_i^n\right), \tag{60}$$

$$u_i^{n+1} = \frac{1}{2}\left(u_i^n + R\left(\nu\Delta t\right) u_i^{(1)} + \frac{a\Delta t}{\Delta x}\left(u_{i-1}^{(1)} - u_i^{(1)}\right)\right) \tag{61}$$

with a relaxation factor $R(z)$, where $z = \nu\Delta t > 0$. A short calculation gives the requirements $R(0) = 1$, $R'(0) = -1$, and $R''(0) = 0$ for $R(z)$ in order to obtain an overall second order time accuracy for (59). The presence of the relaxation changes the CFL condition of the scheme. A von Neumann stability analysis leads to the amplification factor

$$G\left(\xi; z, c\right) = \frac{1}{2}\left(1 + \left(R\left(z\right) + \mathbf{i}\, c \sin\xi + c\left(\cos\xi - 1\right)\right)^2\right) \tag{62}$$

with $z = \nu\Delta t$ and the Courant number $c = a\Delta t/\Delta x$. A sufficient stability condition is $\max_{\xi\in[-\pi,\pi]} \left\|R\left(z\right) + \mathbf{i}\, c \sin\xi + c\left(\cos\xi - 1\right)\right\| \leq 1$ from which we calculate $-1 \leq R\left(z\right) \leq 1$, $c \geq 0$, and

$$c + \frac{1 - R\left(z\right)}{2} \leq 1 \tag{63}$$

as enhanced CFL condition.

For $R(z) \equiv 1$ the stability condition reduces to the classical condition $c \leq 1$. The simple Euler method is given by $R(z) = 1 - z$ and requires small time steps for large ν. To catch the decay of the analytical equation and produce a stable method the relaxation factor should satisfy $R(z) > 0$ and $\lim_{z\to\infty} R(z) = 0$. We propose to use

$$R(z) = \frac{1}{1 - z + z^2} \tag{64}$$

as the stable relaxation factor. It satisfies the order conditions and is decaying to zero. We note that this allows $c \approx \frac{1}{2}$ independent of the relaxation time $1/\nu$.

To incorporate the relaxation factor into (47) we use the single update

$$\mathcal{H}(W^n, \Delta t)|_i = U(\mathcal{P}(W_i^n, \Delta t)) + \frac{\Delta t}{\Delta x}\left(\tilde{F}^{HLL}_{i-\frac{1}{2}} - \tilde{F}^{HLL}_{i+\frac{1}{2}}\right) \tag{65}$$

with the relaxation operator

$$\mathcal{P}(W_i^n, \Delta t) = \begin{pmatrix} (\rho,\, v_x,\, v_y,\, p)^T \\ R(\nu\Delta t)(p_x - p) + p \\ R(\nu\Delta t)(p_y - p) + p \\ R(\nu\Delta t)\,\sigma \\ R\left(\frac{2}{3}\nu\Delta t\right) q_x \\ R\left(\frac{2}{3}\nu\Delta t\right) q_y \end{pmatrix} \tag{66}$$

directly applied to the primitive variables following the equations (58). The Heun time integration (48) together with (65) then provides a stabilized second order coupled transport-relaxation update.

4.4. Dissipative fluxes. It remains to incorporate the dissipative gradient fluxes (31) and (32) into the numerical method. Since these gradients introduce second order spatial derivatives, the structure of the equations without relaxation corresponds to a scalar advection-diffusion equation

$$\partial_t u + a\partial_x u = \mu\partial_{xx} u \tag{67}$$

with a diffusion coefficient $\mu > 0$. The discretization of the second order derivative introduces a stiffness to the system which increases for finer grids or larger values of μ. In many situations the usage of implicit time integrations is an appropriate choice, especially if the operators are split into a fractional step method.

Here we will employ an explicit discretization of the diffusive terms added to the hyperbolic flux for the sake of implementational simplicity. To some extent the problem of stiffness can be relaxed by use of *viscous* or *full upwinding*. This stabilizes the explicit method for Knudsen numbers $Kn < 1$ on moderately refined grids.

The stability for explicit schemes for (67) depends on the value of the characteristic number $\kappa = 2\mu/(|a|\,\Delta x)$ which corresponds to an inverse grid Reynolds number. In a classical method the hyperbolic and parabolic parts of the diffusive flux $F[u] = au - \mu\partial_x u$ are treated differently. The hyperbolic part $a\,u$ is upwinded,

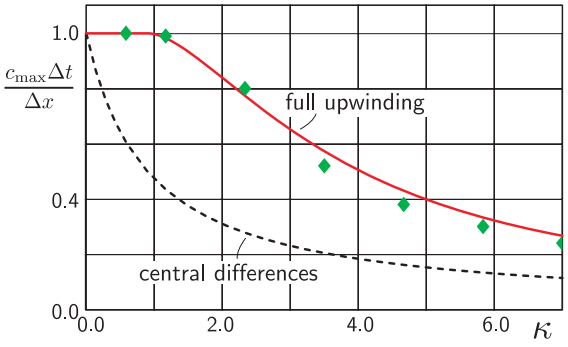

FIG. 3. *Stability condition of the explicit fully upwinded method (solid line) and an explicit method based on central differences (dashed line). The dots represent marginally stable time step sizes for the dissipative HLL flux. The dots follow the fully upwinded method, allowing a bigger time step than central differences.*

while the gradient is approximated by central differences. This leads to the stability condition

$$|c| \leq \frac{1}{1+\kappa} \tag{68}$$

for the Courant number $c = a\Delta t/\Delta x$. If, however, the gradient is upwinded as well, the resulting numerical flux for (67) has the form

$$\tilde{F}^{\text{FullUp}}_{i+\frac{1}{2}} = \begin{cases} au^n_i - \mu\left(\delta_x u\right)_i, & a > 0, \\ au^n_{i+1} - \mu\left(\delta_x u\right)_{i+1}, & a < 0, \end{cases} \tag{69}$$

where $\delta_x u$ is the cell gradient based on some reconstruction. This is easy to implement since the gradient from the reconstruction has usually been computed for the hyperbolic part. The method follows the idea that the upwind direction at an interface determines the cell which all the information should be taken from, including the state variable itself and its gradient. This method is discussed in [45]. The stability condition is now given in the form

$$|c| \leq K^{(\text{crit})}(\kappa) \approx \begin{cases} 1, & \kappa \leq 1, \\ 1.15 - 0.15\kappa, & 1 < \kappa < \kappa_0, \\ \frac{10+4\left(\kappa+\sqrt{6+4\kappa}\right)}{(1+2\kappa)^2} & \text{else} \end{cases} \tag{70}$$

with a decreasing function $K^{(\text{crit})}$ with $\kappa_0 \approx 4.142$. $K^{(\text{crit})}$ approximates an implicitly given function in [45].

The stability condition (70) for the fully upwinded case allows larger time steps than the classical method (68) with symmetric central differences for all κ. The stability gain is most pronounced in the relevant range $1 \leq \kappa \leq 10$. In that range the time step may be up to three times bigger. Figure 3 shows the marginal stable value for c for full upwinding (solid line) and central differences (dashed line). The stability gain due to full upwinding is clearly visible in the figure.

The question is how to extend the flux (69) to a system of equations with nonlinear flux. If all eigenvalues of the matrix (40) have the same sign, the extension is straightforward. Hyperbolic flux and the gradients can be evaluated at the upwind side of the cell interface. However, if the characteristic speeds point in both directions,

the upwinding should be performed according to the decomposition into characteristic variables given by the eigenvectors of (40). Since such a decomposition is not available in the current method we propose using an averaging of the gradients according to the HLL weights. The coefficients $\alpha^{(0,1)}$ of the HLL solver (90) are built such that the flux is upwinded once the information flow is unidirectional. We propose simply incorporating the gradients into the evaluation of the flux function inside the HLL solver to obtain a dissipative numerical flux

$$\tilde{F}^{HLLD}\left(W_L,(\delta W)_L,W_R,(\delta W)_R\right)=\frac{1+\alpha^{(0)}}{2}F\left(W_L,(\delta W)_L\right)+\frac{1-\alpha^{(0)}}{2}F\left(W_R,(\delta W)_R\right)+\frac{\alpha^{(1)}}{2}\left(U\left(W_R\right)-U\left(W_L\right)\right). \tag{71}$$

The discrete gradients δW follow from the reconstruction (86) and enter the full flux $\mathbf{F}$ from (46). In the case of perfectly symmetric eigenvalues the fluxes are averaged, which results in central differences for the gradients. The numerical flux will be used in the single update (47) which enters the Heun method (48). Note that the gradient expressions in (31) and (32) require both x- and y-derivatives also for the calculation of the flux in a single direction.

To verify the stability properties of the full nonlinear scheme (71) empirically we conduct various computations with increasing time steps for different grid sizes. For each grid size, the time step at which instability arises is recorded. The value of κ has been obtained as the maximal value of

$$\kappa=\frac{4\theta}{\nu\,\lambda_{\max}\,\Delta x} \tag{72}$$

for all interfaces. Note that in dimensionless formulation κ is proportional to $Kn/\Delta x$. For the numerical test smooth initial conditions were chosen as described in section 5.1 with $Kn=0.05$ and end time $t=0.4$. Figure 3 shows the marginally stable time steps as dots plotted over κ. The points follow the stability curve (70) of the fully upwinded scheme, which suggests that this stability condition is indeed valid for the current nonlinear extension as well. Hence, the stability condition for the flux (71) reads

$$\frac{\lambda_{\max}^{(x)}\Delta t}{\Delta x\,K^{(\mathrm{crit})}(\kappa)}\leq 1, \tag{73}$$

which replaces the standard CFL condition.

In [45] also the accuracy of the fully upwinded method (69) was investigated. Since the diffusive gradients are approximated on a one-sided basis their accuracy formally drops to first order. However, it was shown that the method shows some kind of superconvergence and shows second order behavior for small values of κ. This can also be observed in the current implementation; see below.

4.5. Two-dimensional method. In two-dimensional calculations the dimensions are often considered separately, and a Godunov or Strang splitting method is employed [24]. Here we use the additive splitting for better multidimensional coupling. The full two-dimensional update based on (65) with (71) has the form

$$\mathcal{H}\left(W^n,\Delta t\right)|_{i,j}=U\left(\mathcal{P}\left(W^n_{i,j},\Delta t\right)\right)+\frac{\Delta t}{\Delta x}\left(\tilde{F}^{HLLD}_{i-\frac{1}{2},j}-\tilde{F}^{HLLD}_{i+\frac{1}{2},j}\right)+\frac{\Delta t}{\Delta y}\left(\tilde{G}^{HLLD}_{i,j-\frac{1}{2}}-\tilde{G}^{HLLD}_{i,j+\frac{1}{2}}\right). \tag{74}$$

The numerical flux in the y-direction $\tilde{G}^{HLLD}_{i,j+\frac{1}{2}}\left(W_B, W_T\right)$ is the direct analogue to the numerical flux in the x-direction described in (71). The dependence of the numerical flux is given by

$$\tilde{F}^{HLLD}_{i+\frac{1}{2},j} = \tilde{F}^{HLLD}\left(W^{(-)}_{i+\frac{1}{2},j}, (\delta W)_{i,j}\,, W^{(+)}_{i+\frac{1}{2},j}, (\delta W)_{i+1,j}\right), \tag{75}$$

which is entirely based on primitive variables and their gradients. Finally, the second order Heun time integration (48) is used as before.

This update suffers from a more restrictive time step condition $\lambda^{(x)}_{\max} + \lambda^{(y)}_{\max} \leq 1$ (see [14]), which could be overcome by using multidimensional corrections. They are not considered here. The final stability is a combination of (63) and (73) in two dimensions. We use

$$\frac{\lambda^{(x)}_{\max}\Delta t}{\Delta x\, K^{(\mathrm{crit})}(\frac{4\theta}{\nu\,\lambda^{(x)}_{\max}\,\Delta x})} + \frac{\lambda^{(y)}_{\max}\Delta t}{\Delta y\, K^{(\mathrm{crit})}(\frac{4\theta}{\nu\,\lambda^{(y)}_{\max}\,\Delta y})} + \frac{1 - H\left(-\frac{2}{3}\nu\Delta t\right)}{2} \leq CFL \tag{76}$$

with $H\left(z\right)$ from (64) and $K^{(\mathrm{crit})}\left(\kappa\right)$ from (70). In a simulation the number $CFL < 1$ has to be chosen as generalized CFL number. The time step is adapted after each time step to satisfy (76).

5. Test calculations. In this section we will demonstrate the capability of the proposed method for the R13 system in several numerical experiment. Studies of empirical order of convergence are conducted.

In addition we will compare the physical behavior of the solutions with the result of the NSF system. This will provide an insight into the relevance of the higher order contributions of the regularized 13-moment equations at higher Knudsen numbers. The results of the NSF system are obtained with a numerical method which resembles the method described in the last section.

All simulations will be based on the nondimensional equations for Maxwell molecules in which the collision frequency ν is replaced by $\frac{\rho}{Kn}$ in (31)–(33). The maximal speeds were calculated using (50).

5.1. Empirical order of convergence. Exact analytical solutions of the R13 equations are available only for strongly simplified situations and initial conditions. In such solutions most of the coupling and nonlinearity is missed. In order to challenge the entire system and the corresponding numerical method we would like to consider nontrivial initial conditions. The unknown analytical solution is then substituted with a high resolution numerical approximation. In that way, the numerical error of coarse grid approximations is estimated, and the empirical order of accuracy can be calculated.

We choose the L^1-error in the form

$$\left\|err\left(\psi\right)\right\|_1 = \sum_{i=1}^{N_x}\sum_{j=1}^{N_y} \Delta x \Delta y \left|\psi^{(num)}_{i,j} - \psi^{(ex)}(x_i, y_j)\right| \tag{77}$$

and the one-dimensional counterpart. The quantity ψ will be the density field ρ and the field of heat flux component q_x in the following.

In the first example we consider a one-dimensional process. The initial conditions are chosen to be

$$\rho_0\left(x\right) = 2 + \frac{1}{2}\cos\left(\pi x\right), \qquad \mathbf{v}_0\left(x\right) = \begin{pmatrix} 1 + \frac{1}{2}\sin(\pi x) \\ \frac{1}{2}\sin(\pi x) \end{pmatrix} \tag{78}$$

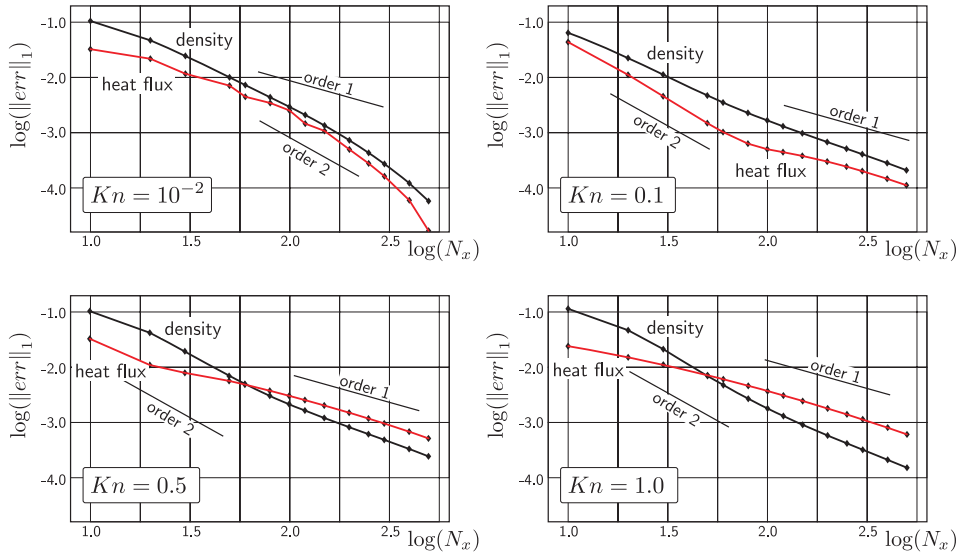

FIG. 4. *Empirical studies of errors of density ρ and heat flux q_x in smooth numerical R13 calculations based on the presented method. The plots show the error curves for a smooth calculation with different Knudsen numbers. The best performance is obtained in the regime of most interest, $Kn = 0.01 \sim 0.5$.*

with $p_0 = 1$. The higher order quantities are set to be at equilibrium

$$(p_x, p_y) = (p_0, p_0)\,, \quad \sigma = 0, \quad (q_x, q_y) = (0, 0) \tag{79}$$

initially. In the process the velocity field introduces compression and expansion into the density which leads to nonuniform directional pressures/temperatures and nonvanishing heat flux. The existence of a y-component of velocity leads to shear stress and heat flux q_y. The end time is $t = 0.4$, and the computational domain is $x \in [-1, 1]$ with periodical boundary conditions. The process is computed with four different values of the Knudsen number, $Kn = 10^{-2}, 0.1, 0.5, 1.0$. The "exact" solution is calculated on a mesh with 2000 cells. The CFL number in (76) was chosen to be 0.9 for all calculations.

Figure 4 shows the errors of coarse grid calculations up to 500 cells. The plots in the figure show the error of density and heat flux for all six choices of the Knudsen number. The results correspond to the predictions of the last section. Best performance in terms of accuracy is achieved at $Kn = 10^{-2}$. In this regime convergence rates higher than second order are observed on fine grids. For larger Knudsen numbers the influence of the dissipative gradient terms grows. For coarse grids the method remains second order in accordance with the findings of [45]. Due to this initial fast convergence the method reaches similar orders of magnitude for the errors in all larger Knudsen number cases.

Two-dimensional case. In two dimensions we consider the smooth solution induced by the initial conditions

$$\rho_0(x) = 2 + \frac{1}{2}\cos(\pi x) + \frac{1}{2}\sin(\pi y)\,, \qquad \mathbf{v}_0(x) = \begin{pmatrix} 1 + \frac{1}{2}\sin(\pi x) + \frac{1}{2}\cos(\pi y) \\ \frac{1}{2}\sin(\pi x) + \frac{1}{2}\cos(\pi y) \end{pmatrix} \tag{80}$$

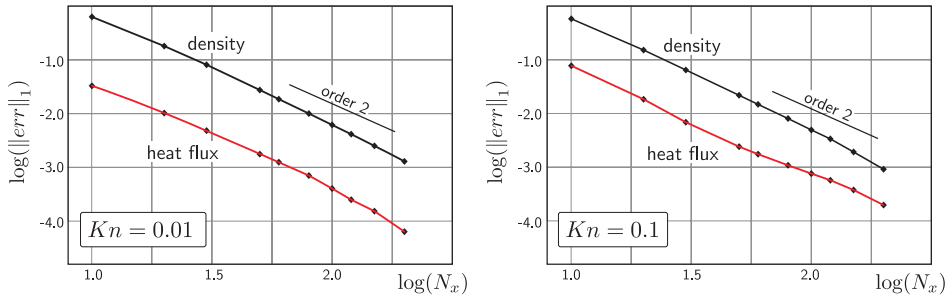

FIG. 5. *Empirical study of the errors of density ρ and heat flux q_x of the R13 system simulated by the numerical method in case of a smooth two-dimensional process. The figure shows results for different Knudsen numbers.*

with $p_0 = 1$ and

$$(p_x, p_y) = (p_0, p_0)\,, \quad \sigma = 0, \quad (q_x, q_y) = (0, 0) \tag{81}$$

at time $t = 0.4$ on the domain $(x, y) \in [-1, 1]^2$ with periodic boundary conditions. The high resolution solution was calculated on a 500×500 grid. Figure 5 shows the results for $Kn = 0.1$ and $Kn = 0.01$ obtained from calculations with a $N_x \times N_y$ grid with $N_x = N_y$. The plots demonstrate the ability of the two-dimensional extension of the numerical method. Second order is clearly achieved.

5.2. Comparison to NSF. The regularized 13-moment system has been demonstrated to describe strong nonequilibrium processes better than classical models such as NSF; see [40], [44]. The differences become more pronounced for higher values of the Knudsen number Kn, i.e., for more rarefied gases or ever smaller length scales. We will consider several processes calculated with R13 and NSF. If deviations arise, the R13 result is expected to be more accurate.

The process originating from the initial conditions given in (78) provides a good example for discussing the possible differences between the R13 and the NSF result. Therefore, the NSF system is solved for the initial condition (78) and different Knudsen numbers. The first major difference to be discussed concerns the initial conditions. Note that in the R13 system we need to prescribe values for the equilibrium variables as well as for the nonequilibrium variables such as shear and heat flux. These variables are set to zero in the example (79). For the NSF system, however, only the equilibrium variables may be prescribed, and the values of shear and heat flux follow immediately from the fields of velocity and temperature according to the constitutive relations (19). Hence, in the present case shear and heat flux will not vanish in the initial conditions for the NSF system. The R13 model allows more precision in the choice of the prescribed fields. Even though the initial conditions for shear and heat flux are different for R13 and NSF both models predict the same behavior in the limit $Kn \to 0$.

Figure 6 shows the result of both models for different fields and different values of the Knudsen number. Due to the increasing Knudsen number the computational domain $[-1, 1]$ can be viewed to represent an ever smaller physical range. The different rows show the fields of full temperature, x-directional temperature, and heat flux in the y-direction. The Knudsen number varies across the columns. The result of R13 and NSF is shown as a dark and light line, respectively. The dashed line in the first

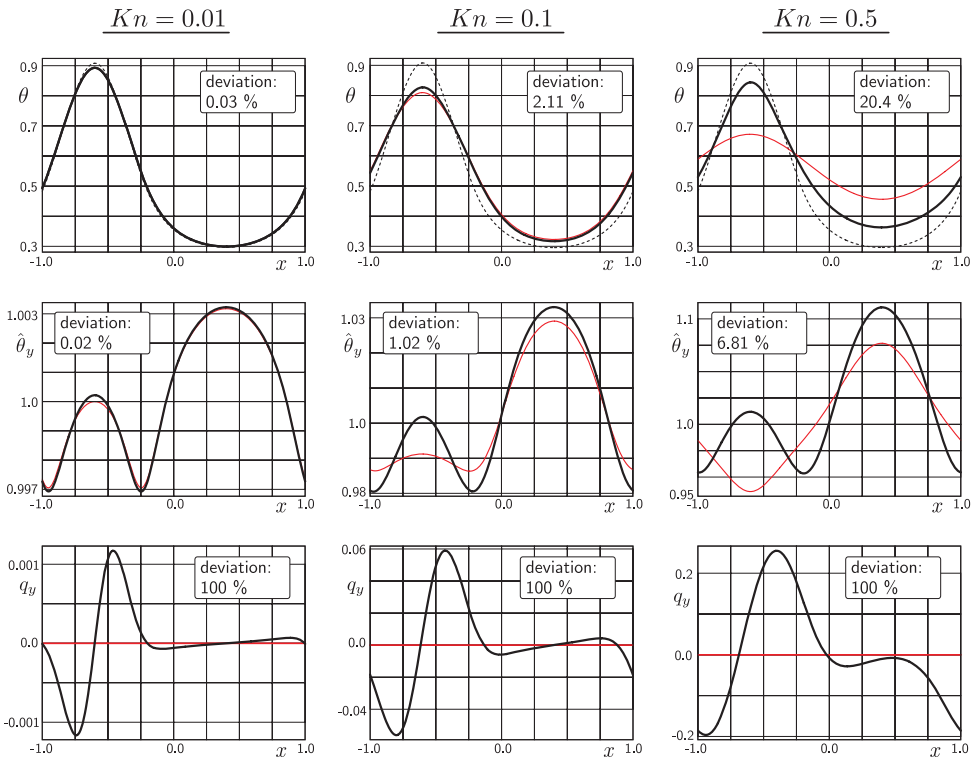

FIG. 6. *Comparison of the process resulting from the initial conditions* (78) *calculated with the R*13 *(dark lines) and NSF (light lines) system for different Knudsen numbers. The result of the Euler system* ($Kn \to 0$) *is given in the first row as reference (dashed line). The deviation is computed as in* (82). *The NSF system is not able to predict a* q_y *heat flux in this case, which leads to a* 100% *deviation for all Knudsen numbers.*

row represents the solution of the Euler equations, i.e., the case $Kn \to 0$. Each plot gives the maximal relative deviation which is calculated from

$$\text{dev}_{rel} = \frac{\left\|\psi^{(R13)} - \psi^{(NSF)}\right\|_\infty}{\left\|\psi^{(R13)}\right\|_\infty} \tag{82}$$

for a field ψ.

In the first column virtually no difference between R13 and NSF is visible in the temperature field and only slightly in the x-temperature. Furthermore, the solutions match the Euler solution. Remarkably, the heat flux q_y gives a 100% deviation even for small Knudsen numbers. The heat flux in the y-direction is induced by the y-velocity field in the R13 system in the absence of any temperature gradient in the y-direction. Hence, the NSF system cannot produce it. In fact, this effect can be shown to be of second order influence, and, indeed, the amplitude of q_y is $\mathcal{O}\left(Kn^2\right)$.

For the larger Knudsen number in the middle column a visible quantitative difference is present, especially in the field of θ_x. In the right column this deviation turns into a qualitative difference. For large Knudsen numbers the dissipation is usually over-estimated by the NSF system. This can be seen in the temperature field which appears strongly damped in the NSF solution.

Riemann problem. The Riemann problem represents a shock-tube experiment in

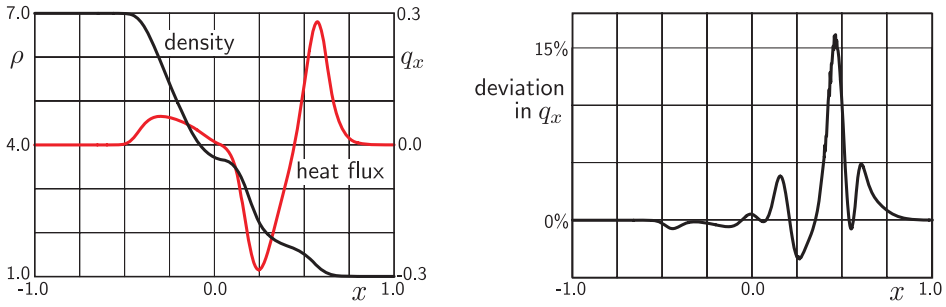

FIG. 7. *Left: density and heat flux in a Riemann problem computed with the R*13 *model. The Knudsen number is* $Kn = 0.02$ *and end time* $t = 0.3$. *Right: relative deviations of the heat flux from the heat flux calculated with the NSF system.*

which a high pressure domain is separated from a low pressure domain by a membrane. The system is initially at rest and in equilibrium, and the membrane is removed at $t = 0$. At later times the typical wave phenomena, such as shock, contact discontinuity, and rarefaction fan, arise. At sufficiently small scales all these waves have diffusive structures incorporating strong dissipation. We present the result of a Riemann problem calculated with the R13 system.

The initial conditions are chosen to be

$$\rho_0(x) = \begin{cases} 7.0, & x < 0, \\ 1.0, & x > 0, \end{cases} \qquad p_0(x) = \begin{cases} 7.0, & x < 0, \\ 1.0, & x > 0, \end{cases} \tag{83}$$

and

$$(v_x, v_y) = (0,0), \quad (p_x(x), p_y(x)) = (p_0(x), p_0(x)), \quad \sigma = 0, \quad (q_x, q_y) = (0,0). \tag{84}$$

The computational domain is $x \in [-1, 1]$ and the end time $t = 0.3$. The Knudsen number controls what physical dimensions correspond to these spatial and temporal values. Due to the strong pressure and density difference the start-up period of the Riemann problem in which the waves develop is accompanied by strong nonequilibrium on small time and space scales. This start-up phase was investigated in [5] using high order moment theories. Here we will focus on moderate scales. We use $Kn = 0.02$ and conclude that the physical range covers approximately 100 mean free paths and the end time corresponds to approximately 15 mean free-flight times.

The left-hand side of Figure 7 shows the fields of density ρ and heat flux q_x in a single plot. The scale of density and heat flux is given in the right- and left-hand side, respectively. The density profile shows the rarefaction fan, the contact "discontinuity," and the shock which have just developed. The heat flux exhibits three peaks, indicating the nonequilibrium attributed to the three waves. The same process can be calculated with the NSF equations, and the relative spatial deviation between $q_x^{(R13)}$ and $q_x^{(NSF)}$ is plotted in the right-hand side of Figure 7. The biggest spike corresponds to the area between the shock and the contact wave which have not yet separated.

6. Microflow example. This section is devoted to a specific flow situation in which a shock wave interacts with a dense microbubble. The example is chosen to demonstrate the ability of the R13 equations for two-dimensional bulk flows in the

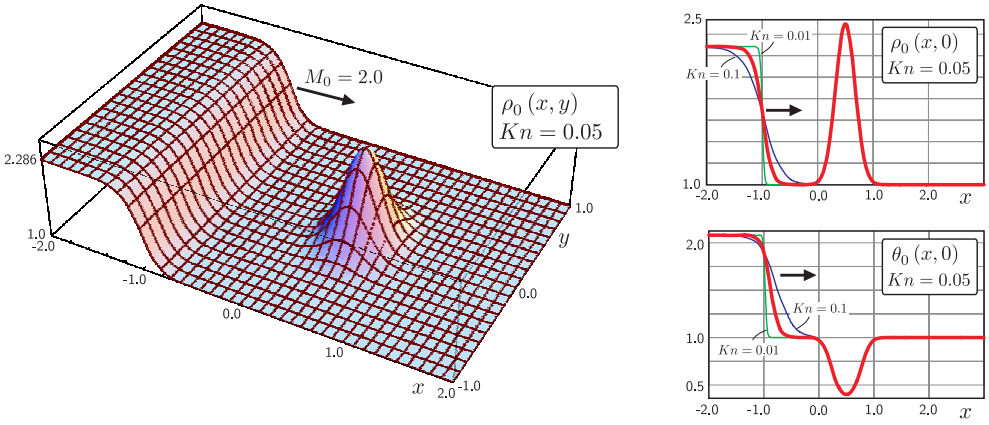

FIG. 8. *Initial conditions for the shock-bubble interaction process. A shock wave profile propagates in the x-direction and hits a dense and cold bubble. The diameter of the bubble is chosen to be decreasing in different simulations, from* 100 *to* 10 *mean free paths. This is realized by using different Knudsen numbers. The right-hand plots show cuts of the initial conditions along* $y = 0$. *Due to the change of spatial scale the shock profile becomes wider for larger Knudsen numbers.*

absence of boundaries. The interaction with boundaries will be investigated elsewhere. The shock-bubble simulation is conducted for decreasing bubble diameter d from $d = 100\lambda_0$ to $d = 10\lambda_0$, where λ_0 is the mean free path. The results are compared to NSF.

6.1. Initial conditions. The scenario of the initial conditions is shown in Figure 8. A shock wave profile is situated with its density barycenter at $x = -1.0$ traveling in the positive x-direction with Mach number $M_0 = 2.0$ into a flow field at rest with $(\rho, \theta, p) = (1, 1, 1)$. Around $(x, y) = (0.5, 0.0)$ a circular density bubble is placed with density distribution

$$\rho(x,y) = 1 + 1.5 \exp\left(-16\left(x^2 + y^2\right)\right) \tag{85}$$

and constant pressure. The exponential is built such that only minimal interaction between the profile and the bubble exist initially. Due to constant pressure the interior of the bubble will be colder than the environment. The entire computational domain is given by $[-2, 3] \times [-1, 1]$.

As above the simulations will be based on dimensionless equations for Maxwell molecules in which only the Knudsen number remains to be specified. For the shock-bubble interaction we choose $Kn = 0.01, 0.05, 0.1$; hence the distance $\Delta x = 1$ corresponds to 100, 20, and 10 mean free paths of the reference state, respectively. Accordingly, the diameter of the dense bubble will decrease its actual physical range. However, the shock wave profile will be initialized in agreement with the Knudsen number. This leads to a broader or thinner profile as indicated in the right plots of Figure 8.

The shock wave profile was computed in a preceding one-dimensional calculation. Starting from discontinuous states given by the Rankine–Hugoniot conditions the time evolution was calculated until the stationary shock profile was fully developed. The resulting profile including the profiles for heat flux and stress were used in the initialization of the shock-bubble problem after appropriate scaling.

The shock-bubble interaction was simulated with the R13 system on 250×100 and

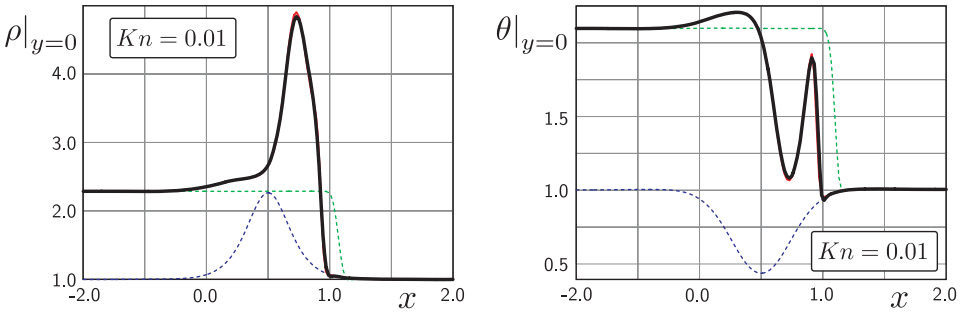

FIG. 9. *Result of the shock-bubble interaction at $t = 0.8$ for the dense case $Kn = 0.01$. The shock front just passes the bubble. In the figure the result of the R13 system (thick line) and of the NSF model (thin line) give essentially the same solution. The dashed lines represent the fields of the shock front and the bubble in the unperturbed case.*

500×200 grid cells up to time $t = 1.2$ at which the shock position is approximately $x = 1.5$. The results of both calculations did not show substantial differences, and the solutions are considered to be converged in sufficient accuracy.

For comparison the whole simulation is repeated using the NSF system. In that case also the shock profile was based on a preceding NSF calculation, since the shock profile differs for both models. As mentioned above any temperature gradient induces an immediate heat flux according to Fourier's law. Hence, for NSF the initial conditions of the shock-bubble simulation consist also of a heat flux inside the bubble. To guarantee a fair comparison by using the same initial conditions this heat flux—according to Fourier—is computed initially for the R13 simulations as well. However, the inclusion of this heat flux exhibits only a little influence on the R13 result.

6.2. Results for the dense limit. The case $Kn = 0.01$ represents the dense or macrolimit which we present here for reference. The result for density and temperature at $t = 0.8$ along $y = 0$ is given in Figure 9 for both NSF and R13. At this scale the solutions of R13 and NSF almost agree, and the solution shape is similar to the result of Euler equations, $Kn \to 0$ (not shown).

In the figure the shock passed through the bubble and reached approximately $x = 1.0$. The profile of both the unperturbed shock wave and density bubble at $t = 0.8$ are shown with dashed lines. Note that the unperturbed bubble melts slowly due to heat conduction. As can be read from the figure the presence of the dense bubble makes the shock slow down and produces a strong density peak behind it. The bubble is compressed and pushed towards the shock. The solution in front of the shock still corresponds to the unperturbed bubble.

6.3. Microcase. At Knudsen numbers larger than 0.01 the solutions of the NSF model and the R13 equations start to deviate more and more. Due to the higher kinetic accuracy of the R13 system we expect its solution to be the physically relevant one.

To give an impression of the distortion of the shock front due to the bubble Figure 10 shows three-dimensional plots of various fields at time $t = 0.9$. The result shown is based on $Kn = 0.5$ and the range $x \in [0, 2] \times [-1, 1]$. However, the plots in the figure use mean free path units. The area of 40×40 mean free paths corresponds approximately to $3 \times 3\,\mu m^2$ for Argon at atmospheric condition. The end time of 18 mean free-flight times corresponds roughly to $0.01\,\mu s$.

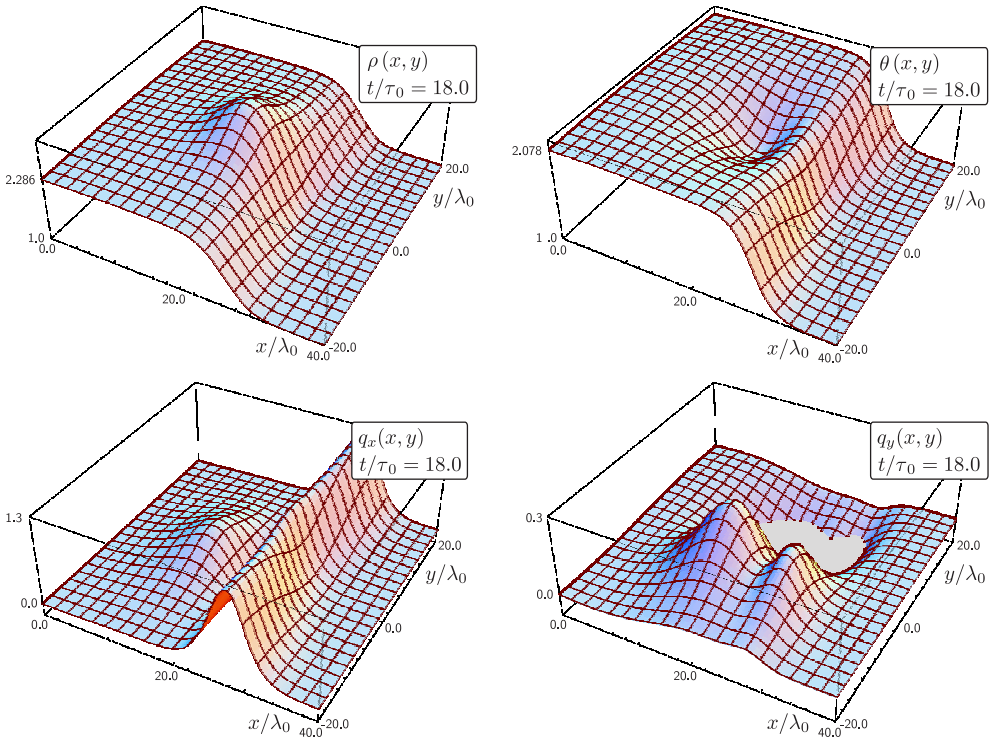

FIG. 10. *Two-dimensional plots of the fields of density ρ, temperature θ, and heat flux (q_x, q_y) for the shock-bubble interaction. The initial diameter of the bubble ranged 20 mean free paths. The shock front started 30 mean free paths in front of the bubble center and passed completely through it at the time shown. λ_0 and τ_0 are the mean free path and the mean free-flight time of the reference state in front of the shock.*

At the time shown in the figure the front has fully passed through the bubble. The bubble is now placed behind the shock. The temperature front is dented due to the interaction. A strong kink is also visible in the soliton shaped heat flux component q_x which interacts with the heat flux inside the bubble. The heat flux component q_y vanishes in the unperturbed shock profile. However, after the interaction with the bubble the distortion excites this heat flux component pointing symmetrically towards the center line. All other fields such as shear and directional temperature exhibit corresponding behavior.

6.4. Comparison. We study the solutions of the R13 system and the NSF equations for the shock-bubble interaction. Any difference must be related to the first order character of the constitutive relations of NSF which becomes most pronounced for larger Knudsen numbers.

At time $t = 0.8$ the shock front is just about to exit the bubble. This situation shows the strongest nonequilibrium and correspondingly the strongest differences between the models. One-dimensional cuts for density ρ, temperature θ, and heat flux (q_x, q_y) in the case $Kn = 0.05$ are shown in Figure 11. Density, temperature, and heat flux component q_x are shown along the center line $y = 0$, while q_y follows $y = -0.4$. The dashed lines in the upper two plots give a reference to the unperturbed fields of the shock front and density bubble, respectively. The solution of the NSF system is shown using thin lines.

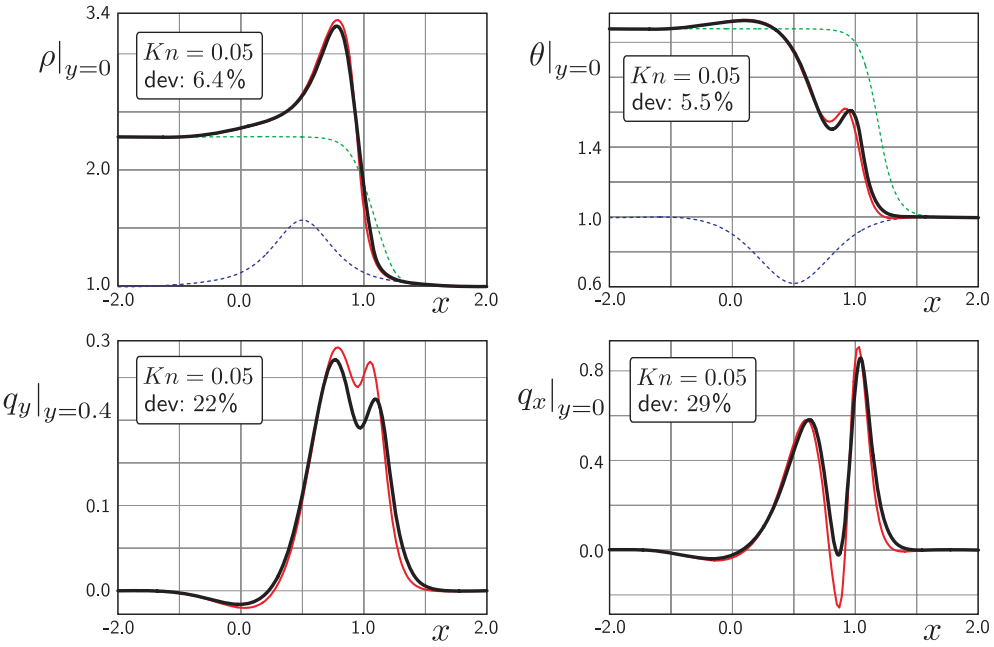

FIG. 11. *Detailed study of the shock-bubble interaction at $t = 0.8$ for the case $Kn = 0.05$. The shock front just passes the bubble. In the figure both the result of the R13 system (thick line) and of the NSF model (thin line) are displayed. The dashed lines in the upper row represent the shock front and the bubble in the unperturbed case.*

In comparison with the dense case $Kn = 0.01$ the density overshoot is much smaller and the nonmonotonicity of the temperature weaker. Generally speaking, the NSF result overestimates the density peak and the heat flux. The maximal deviation between the models defined in (82) is incorporated into each plot. It is maximal for the heat flux with values around 25%. The minimum in the middle of q_x is of special interest. Even though the temperature gradient is positive in this region, the R13 heat flux predicts a positive heat flux. This is possible, since both quantities are decoupled in the model, accounting for the inertia in a developing heat flux. The NSF system lacks this inertia which leads to overestimation.

The differences between the models become even stronger in the case $Kn = 0.1$. At this scale the bubble has an initial diameter of 10 mean free paths. The result at time $t = 0.8$ is displayed in Figure 12 using the same setup as in Figure 11. The density overshoot is further reduced and the shock front loses almost no speed while crossing the bubble, in contrast to the $Kn = 0.01$ case. This is due to the fact that the bubble contains less mass and is also more diffused at high Knudsen numbers; see the graph of the unperturbed field. The NSF solution gives a smeared out temperature field which leads to a mismatch in the actual shock position. The failure of NSF is also manifested in strong 30% deviations in the heat flux.

We note that the differences originate purely from the lack of accurate high order nonequilibrium multiscale modeling in the simple NSF system. In that sense the deviations are a bulk effect and can obviously not be influenced by boundary conditions as in slip models.

7. Conclusion. A numerical method and corresponding numerical simulations have been presented for the two-dimensional regularized 13-moment equations for

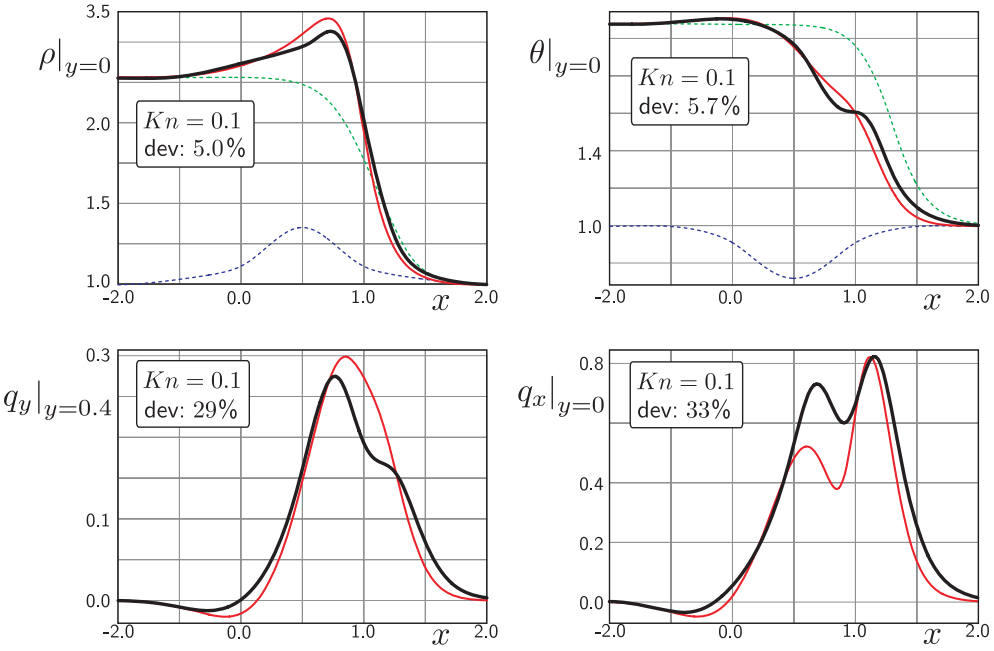

FIG. 12. *Detailed study of the R13 system (thick line) and of the NSF model (thin line) in the shock-bubble interaction at $t = 0.8$ for the case $Kn = 0.1$. The dashed lines in the upper row represent the shock front and the bubble in the unperturbed case. At this scale the NSF equations show wrong results for shock position, strength, and shape.*

rarefied/microflow. In contrast to other fluid models the R13 system models the nonequilibrium dissipation with high accuracy. The two-dimensional equations and their properties have been presented and discussed in detail. The numerical method is derived in a straightforward coupled finite volume approach with stabilized relaxational and dissipative terms. Numerical experiments demonstrate both accuracy and stability properties of the proposed method.

To demonstrate the capabilities of the method and the R13 model a special microflow example has been simulated. The process consisted of an interaction of a shock wave and a microbubble with a diameter of a few mean free paths. Comparison with NSF solutions shows strong deviations in the case where the diameter is below 50 mean free paths.

In future work the present method will be extended to include boundary conditions using a hybrid kinetic/continuum approach. Also, the numerical method will be enhanced to improve asymptotic properties.

Appendix A. Second order HLL flux. We assume a finite volume discretization based on rectangular grid cells with cell centers (x_i, y_i) and mean cell values $U^n_{i,j}$ at time level n. The update itself is performed for the convective variables U of the R13 system, especially the conservative variables density, momentum density, and total energy density. However, it is recommended to conduct the calculations of each time step of the method in primitive variables W. We have $W_i = W(U_i)$ for each cell and calculate the derivative of W from

$$(\delta_x W)_i = \frac{1}{\Delta x}\varphi\left(W_i - W_{i-1}, W_{i+1} - W_i\right). \tag{86}$$

In general φ is a limiter function which avoids oscillations in the reconstructed function for W. For smooth solutions it suffices to use $\varphi(d_1, d_2) = \frac{1}{2}(d_1 + d_2)$, which realizes nonlimited central differences. In the case of, e.g., discontinuous initial data, the van Leer limiter

$$\varphi^{(vanLeer)}(d_1, d_2) = \frac{|d_1|\, d_2 + |d_2|\, d_1}{|d_1| + |d_2|} \tag{87}$$

is used. The discrete gradient of W is denoted by $\delta W = (\delta_x W, \delta_y W)$.

The update for U_i^n uses the conservative intercell flux formulation

$$U_i^{n+1} = U_i^n + \frac{\Delta t}{\Delta x}\left(\tilde{F}^{HLL}\left(W_{i-\frac{1}{2}}^{(-)}, W_{i-\frac{1}{2}}^{(+)}\right) - \tilde{F}^{HLL}\left(W_{i+\frac{1}{2}}^{(-)}, W_{i+\frac{1}{2}}^{(+)}\right)\right), \tag{88}$$

where the values which enter the numerical flux function are the reconstructed values given by

$$W_{i+\frac{1}{2}}^{(-)} = W_i + \frac{\Delta x}{2}(\delta_x W)_i, \qquad W_{i+\frac{1}{2}}^{(+)} = W_{i+1} - \frac{\Delta x}{2}(\delta_x W)_{i+1}. \tag{89}$$

There are many options for the numerical flux function $\tilde{F}(W_L, W_R)$. Apart from standard choices the dissertation [8] investigated Roe solvers for higher moment methods. Approximate Riemann solvers are difficult to construct in the present case due to the thread of possible loss of hyperbolicity. However, the numerical diffusion is minimal in those solvers. Here we use the HLL approximate Riemann solvers from [12] which require only flux evaluations and a fastest wave speed. This flux also offers an efficient way to incorporate the dissipative fluxes.

For completeness, we present the HLL flux given by

$$\tilde{F}^{HLL}(W_L, W_R) = \frac{1+\alpha^{(0)}}{2}F^{(0)}(W_L) + \frac{1-\alpha^{(0)}}{2}F^{(0)}(W_R) + \frac{\alpha^{(1)}}{2}\left(U(W_R) - U(W_L)\right) \tag{90}$$

with

$$\alpha^{(0)} = \frac{|\lambda_L| - |\lambda_R|}{\lambda_L - \lambda_R}, \qquad \alpha^{(1)} = \frac{|\lambda_L|\,\lambda_R - |\lambda_R|\,\lambda_L}{\lambda_L - \lambda_R}. \tag{91}$$

We use $\lambda_R = v_x^{(R)} + c_{\max}^{(R)}$ and $\lambda_L = v_x^{(L)} - c_{\max}^{(L)}$ as maximal characteristic speeds to the right and to the left, respectively. In principle these values need to be calculated from (41). A maximal speed is given by $\lambda_{\max} = \max(\lambda_L, \lambda_R)$.

REFERENCES

[1] A. Abdulle and A. A. Medovikov, *Second order Chebyshev methods based on orthogonal polynomials*, Numer. Math., 90 (2001), pp. 1–18.

[2] R. K. Agarwal, K. Y. Yun, and R. Balakrishnan, *Beyond Navier-Stokes: Burnett equations for flows in the continuum-transition regime*, Phys. Fluids, 13 (2001), pp. 3061–3085.

[3] R. K. Agarwal, K. Y. Yun, and R. Balakrishnan, *Erratum: Beyond Navier-Stokes: Burnett equations for flows in the continuum-transition regime*, Phys. Fluids, 14 (2002), p. 1818.

[4] J. D. Au, *Lösung nichtlinearer Probleme in der Erweiterten Thermodynamik*, Ph.D. dissertation, Technical University of Berlin, Berlin, Germany, 2001.

[5] J. D. Au, M. Torrilhon, and W. Weiss, *The shock tube study in extended thermodynamics*, Phys. Fluids, 13 (2001), pp. 2423–2432.

[6] G. A. Bird, *Molecular Gas Dynamics and the Direct Simulation of Gas Flows*, 2nd ed., Oxford University Press, New York, 1998.
[7] A. V. Bobylev, *The Chapman-Enskog and Grad methods for solving the Boltzmann equation*, Soviet Phys. Dokl., 27 (1982), pp. 29–31.
[8] S. Brown, *Approximate Riemann Solvers for Moment Models of Dilute Gases*, Ph.D. dissertation, University of Michigan, Ann Arbor, MI, 1999.
[9] R. E. Caflisch, S. Jin, and G. Russo, *Uniformly accurate schemes for hyperbolic systems with relaxation*, SIAM J. Numer. Anal., 34 (1997), pp. 246–281.
[10] G. V. Candler, S. Nijhawan, D. Bose, and I. D. Boyd, *A multiple translational temperature gas dynamics model*, Phys. Fluids, 6 (1994), pp. 3776–3786.
[11] S. Chapman and T. G. Cowling, *The Mathematical Theory of Non-Uniform Gases*, Cambridge University Press, Cambridge, UK, 1970.
[12] B. Einfeldt, *On Godunov-type methods for gas dynamics*, SIAM J. Numer. Anal., 25 (1988), pp. 294–318.
[13] B.-C. Eu, *A modified moment method and irreversible thermodynamics*, J. Chem. Phys., 73 (1980), pp. 2958–2969.
[14] E. Godlewski and P.-A. Raviart, *Numerical Approximation of Hyperbolic Systems of Conservation Laws*, Springer, New York, 1996.
[15] H. Grad, *On the kinetic theory of rarefied gases*, Comm. Pure Appl. Math., 2 (1949), pp. 331–407.
[16] H. Grad, *Principles of the kinetic theory of gases*, in Handbuch der Physik, Vol. 12, S. Flügge, ed., Springer, Berlin, 1958.
[17] S. Jin, *Runge-Kutta methods for hyperbolic conservation laws with stiff relaxation terms*, J. Comput. Phys., 122 (1995), pp. 51–67.
[18] S. Jin and M. Slemrod, *Regularization of the Burnett equations via relaxation*, J. Statist. Phys., 103 (2001), pp. 1009–1033.
[19] S. Jin, L. Pareschi, and M. Slemrod, *A relaxation scheme for solving the Boltzmann equation based on the Chapman-Enskog expansion*, Acta Math. Appl. Sin. Engl. Ser., 18 (2002), pp. 37–62.
[20] D. Jou, J. Casas-Vazquez, and G. Lebon, *Extended Irreversible Thermodynamics*, 2nd ed., Springer, Berlin, 1996.
[21] M. Junk, *Domain of definition of Levermore's five-moment system*, J. Statist. Phys., 93 (1998), pp. 1143–1167.
[22] I. V. Karlin, A. N. Gorban, G. Dukek, and T. F. Nonnenmacher, *Dynamic correction to moment approximations*, Phys. Rev. E (3), 57 (1998), pp. 1668–1672.
[23] G. E. Karniadakis and A. Beskok, *Micro Flows: Fundamentals and Simulation*, Springer, New York, 2001.
[24] R. J. LeVeque, *Finite Volume Methods for Hyperbolic Problems*, Cambridge University Press, Cambridge, UK, 2002.
[25] R. J. LeVeque, *Balancing source terms and flux gradients in high-resolution Godunov methods: The quasi-steady wave-propagation algorithm*, J. Comput. Phys., 146 (1998), pp. 346–365.
[26] C. D. Levermore, *Moment closure hierarchies for kinetic theories*, J. Statist. Phys., 83 (1996), pp. 1021–1065.
[27] S. F. Liotta, V. Romano, and G. Russo, *Central schemes for balance laws of relaxation type*, SIAM J. Numer. Anal., 38 (2000), pp. 1337–1356.
[28] D. A. Lockerby and J. M. Reese, *High-resolution Burnett simulations of micro Couette flow and heat transfer*, J. Comput. Phys., 188 (2003), pp. 333–347.
[29] I. Müller and T. Ruggeri, *Rational Extended Thermodynamics*, 2nd ed., Springer Tracts Nat. Philos. 37, Springer, New York, 1998.
[30] I. Müller, D. Reitebuch, and W. Weiss, *Extended thermodynamics—Consistent in order of magnitude*, Contin. Mech. Thermodyn., 15 (2003), pp. 411–425.
[31] R.-S. Myong, *A computational method for Eu's generalized hydrodynamic equations of rarefied and microscale gasdynamics*, J. Comput. Phys., 168 (2001), pp. 47–72.
[32] L. Pareschi and G. Russo, *Implicit-explicit Runge-Kutta schemes and applications to hyperbolic systems with relaxation*, J. Sci. Comput., 25 (2004), pp. 129–155.
[33] R. Roveda, D. B. Goldstein, and P. L. Varghese, *Hybrid Euler/particle approach for continuum/rarefied flow*, J. Spacecr. Rockets, 35 (1998), pp. 258–265.
[34] S. Seeger and H. Hoffmann, *The cumulant method in computational kinetic theory*, Contin. Mech. Thermodyn., 12 (2000), pp. 403–421.
[35] Y. Sone, *Kinetic Theory and Fluid Dynamics*, Birkhäuser, Basel, 2002.
[36] H. Struchtrup, *Macroscopic Transport Equations for Rarefied Gas Flows*, Interaction of Mechanics and Mathematics XIV, Springer, New York, 2005.

[37] H. Struchtrup, *Heat transfer in the transition regime: Solution of boundary value problems for Grad's moment equations via kinetic schemes*, Phys. Rev. E (3), 65 (2002), 041204.
[38] H. Struchtrup, *Stable transport equations for rarefied gases at high orders in the Knudsen number*, Phys. Fluids, 16 (2004), pp. 3921–3934.
[39] H. Struchtrup, *Derivation of* 13 *moment equations for rarefied gas flow to second order accuracy for arbitrary interaction potentials*, Multiscale Model. Simul., 3 (2005), pp. 221–243.
[40] H. Struchtrup and M. Torrilhon, *Regularization of Grad's* 13*-moment-equations: Derivation and linear analysis*, Phys. Fluids, 15 (2003), pp. 2668–2680.
[41] Q. Sun, I. D. Boyd, and G. V. Candler, *A hybrid continuum/particle approach for modeling subsonic, rarefied gas flows*, J. Comput. Phys., 194 (2004), pp. 256–277.
[42] Y. Suzuki and B. van Leer, *Application of the* 10*-moment model to MEMS flows*, in Proceedings of the 43rd AIAA Aerospace Sciences Meeting and Exhibit, AIAA paper 2005-1398, 2005.
[43] M. Torrilhon, *Characteristic waves and dissipation in the* 13*-moment-case*, Contin. Mech. Thermodyn., 12 (2000), pp. 289–301.
[44] M. Torrilhon and H. Struchtrup, *Regularized* 13*-moment-equations: Shock structure calculations and comparison to Burnett models*, J. Fluid Mech., 513 (2004), pp. 171–198.
[45] M. Torrilhon and K. Xu, *Consistency and stability of kinetic upwinding for advection-diffusion equation*, IMA J. Numer. Anal., to appear.
[46] W. G. Vincenti and C. H. Kruger, Jr., *Introduction to Physical Gas Dynamics*, Wiley, New York, 1965.
[47] K. Xu, *Regularization of the Chapman-Enskog expansion and its description of shock structure*, Phys. Fluids, 14 (2002), pp. L17–L20.
[48] K. Xu and Z.-H. Li, *Microchannel flow in the slip regime: Gas-kinetic BGK-Burnett solutions*, J. Fluid Mech., 513 (2004), pp. 87–110.
[49] X. Zhong, R. W. MacCormack, and D. R. Chapman, *Stabilization of the Burnett equations and applications to hypersonic flows*, AIAA J., 31 (1993), pp. 1036–1043.